NASA TECHNICAL NOTE

NASA TN D-5312

NASA TN D-5312

AN ANALOG COMPUTER STUDY OF THE LOW-FREQUENCY FLOW DYNAMICS OF TWO NUCLEAR-ROCKET COLD-FLOW ENGINE SYSTEMS

by Harry W. Fox, Jr., and Ronald J. Blaha

Lewis Research Center
Cleveland, Ohio

NATIONAL AERONAUTICS AND SPACE ADMINISTRATION • WASHINGTON, D. C. • JULY 1969

AN ANALOG COMPUTER STUDY OF THE LOW-FREQUENCY FLOW DYNAMICS OF TWO NUCLEAR-ROCKET COLD-FLOW ENGINE SYSTEMS

By Harry W. Fox, Jr., and Ronald J. Blaha

Lewis Research Center
Cleveland, Ohio

NATIONAL AERONAUTICS AND SPACE ADMINISTRATION

For sale by the Clearinghouse for Federal Scientific and Technical Information
Springfield, Virginia 22151 – CFSTI price $3.00

ABSTRACT

An analog computer study is made of the low-frequency flow dynamics observed with liquid hydrogen flowing in two different nuclear-rocket cold-flow (unfueled) engine systems. The prediction of the low-frequency response depends largely upon the generation of the proper mass-flow storage in the system. This is achieved by relating, in the model lumping, the average values of fluid enthalpy and a certain thermodynamic fluid property. A two-phase state equation is derived for thermodynamic equilibrium between the gas and liquid phases. Parametric studies are made which demonstrate the effect of the pump characteristics on the flow damping.

TABLE OF CONTENTS

AN ANALOG COMPUTER STUDY OF THE LOW-FREQUENCY FLOW DYNAMICS OF TWO NUCLEAR-ROCKET COLD-FLOW ENGINE SYSTEMS

by Harry W. Fox. Jr., and Ronald J. Blaha

Lewis Research Center

SUMMARY

A study is made of the mechanisms which govern the low-frequency flow dynamics observed with liquid hydrogen flowing in two nuclear-rocket cold-flow (unfueled) engine systems. An analog computer model is used which is characterized by three fluid-lumps: a liquid lump, a two-phase lump, and a gas lump. The positions of the fluid-lump boundaries are calculated in high-speed repetitive operation and are allowed to shift in time.

A two-phase equation of state is derived for the case when thermodynamic equilibrium may be assumed between the gas and liquid phases. The form of the equation is

$$P_{2p} = \rho_{2p}[\alpha(P_{2p}) + \beta(P_{2p})\, h_{2p}]$$

where P_{2p} is the two-phase pressure, ρ_{2p} is the two-phase density, h_{2p} is the two-phase enthalpy, and α and β are coefficients which are functions of pressure.

An important result of the study is that prediction of the low-frequency response ($\leq$5 Hz) depends largely on the generation of the proper mass-flow storage in the system. It is found that most of the mass-flow storage occurs in two-phase regions of very low mass quality. A good representation of this mass-flow accumulation, in the model lumping, is achieved by relating the average fluid enthalpy to the average value of the thermodynamic property $[\partial\rho/\partial P]_h$, which is the partial derivative of density with respect to pressure (enthalpy held constant).

Parametric studies demonstrate that the pump operating characteristics can significantly affect the system damping. And further, it is shown that operation on positive pump-map slopes reduces the overall system damping.

INTRODUCTION

A nuclear-rocket engine in space probably will use no special startup equipment. Instead, it will rely on a bootstrap starting procedure. The bootstrap technique has been used successfully to start chemical-rocket engines, but there are significant differences in the nuclear-engine bootstrap.

One difference is the much longer time for the nuclear rocket to be brought to power. Also, only the hydrogen propellant is used, and it follows a more complex flow path in the nuclear rocket. In addition there is a lack of precise knowledge of two-phase hydrogen flow and boiling phenomena. All these factors caused concern that intolerable flow oscillations might occur during the nuclear-engine startup. Therefore, full-scale experimental tests of the bootstrap of a nuclear-rocket engine were undertaken.

In this report, an analog computer model is used to study the mechanisms which govern the low-frequency flow dynamics observed with liquid hydrogen flowing in two different nuclear-rocket cold-flow engine systems (the nuclear-rocket engine with an axial pump and with a radial pump). A previous analytical simulation of the entire engine system with an axial pump resulted in a good overall representation (ref. 1). The model, however, was unable to simulate the observed low-frequency flow dynamics. It was concluded in reference 1 that this was due mainly to the lack of an adequate two-phase equation of state. The purposes of this study, therefore, are (1) to generate an adequate two-phase state equation of the form $P = P(\rho, h)$, and (2) to formulate a modeling technique which predicts the low-frequency flow dynamics observed in the experimental tests.

The goal of previous analytical treatments has been to develop a mathematical model to simulate the nuclear-rocket engine startup. The system was studied by dividing the model into fixed spatial lumps, each representing a specific hardware component of the research apparatus shown in figure 1. These lumps were then grouped (as in fig. 2) into a system block diagram composed of a pump, feedline, nozzle-coolant tubes, reflector, core, thrust nozzle, turbine-bleed line, turbine-power-control valve, and turbine. The lumping was done in this manner to take advantage of system geometry and data sensor locations and also to limit the amount of necessary analog computing equipment.

The differential equations describing each lump were written and then programmed on the analog computer. In general, the experimental data were matched to within 10 to 25 percent except during the periods of large flow transients (ref. 1). This quasi-steady-state model was unable to simulate the observed low-frequency flow transients. There was a lack of a convenient expression relating pressure to a function of density and enthalpy for the two-phase fluid. This forced the dropping of certain time derivatives in the two-phase lump equations. The low-frequency dynamics that are characteristic of the two-phase lump were thus removed.

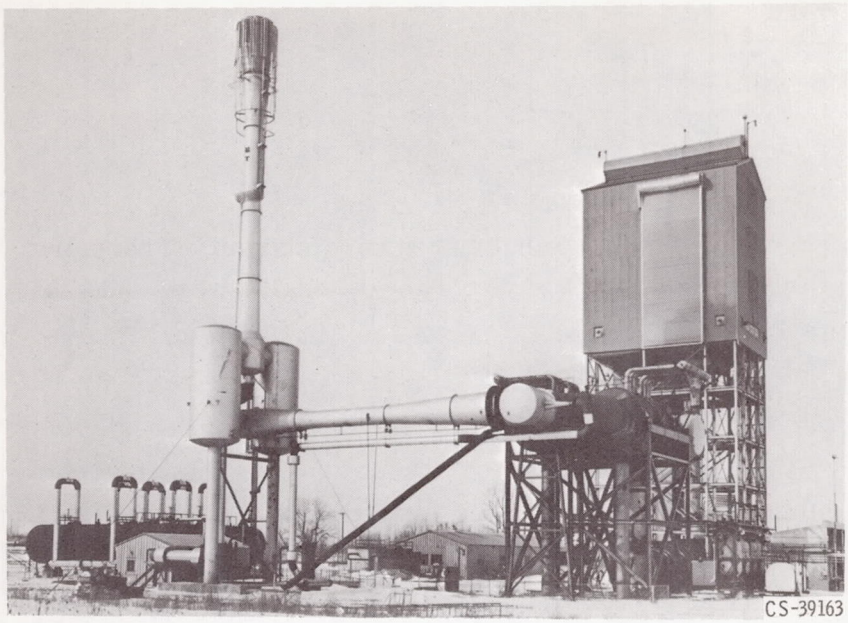

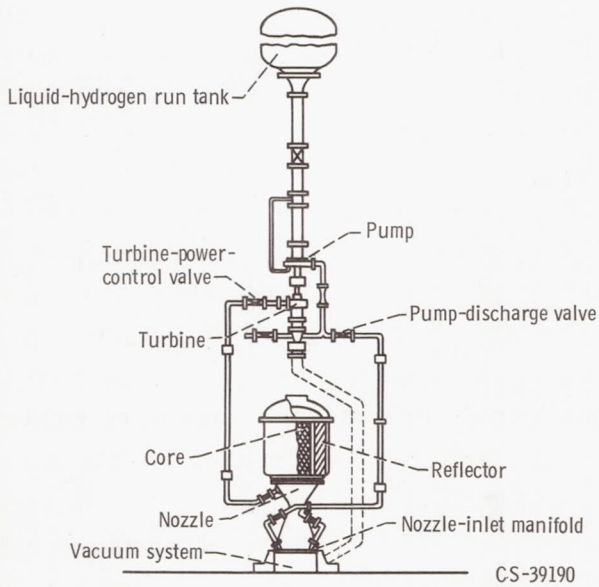

Figure 1. - Axial-pump nuclear-rocket cold-flow test facility.

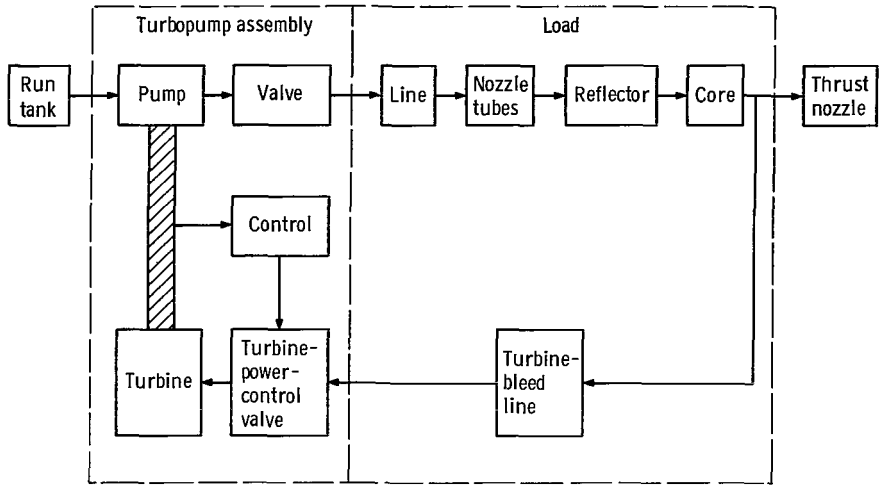

Figure 2. - System block diagram.

In this study of the low-frequency flow dynamics the analog computer model used is a special simplication of the model used in reference 1. The present model is characterized by three fluid-lumps: a liquid lump, a two-phase lump, and a gas lump. The three fluid-lumps represent the system from the pump discharge to the core exit.

The concept of the model is based on the observed state of the fluid throughout the system during the course of an experimental run. With liquid hydrogen flowing into the system, the material of the components begin to cool by giving up latent heat to the fluid. Throughout every experimental test, a definite, but changing, portion of the system contained two-phase fluid. The preceding portion was all liquid, while the remaining portion downstream was all gas (see fig. 3). As the run proceeded and the system cooled, the two-phase section moved downstream.

Differential equations are written for a liquid fluid-lump, a two-phase fluid-lump and a gas fluid-lump. In contrast to a conventional lump fixed in space, each fluid-lump is characterized by one or two variable boundaries which may shift through space (the system). The positions of these moving boundaries are calculated in high-speed, repet-

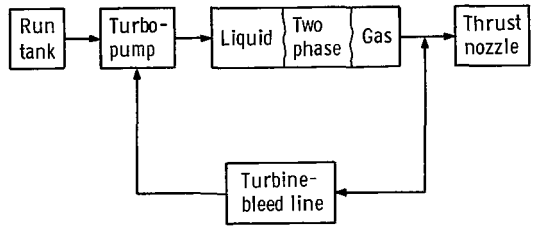

Figure 3. - Simplified model showing variation of fluid state throughout system.

itive operation on the analog computer.

The three-fluid-lump system is bounded on the upstream side by a run tank, inlet feedline, and pump. The speed of the pump is a programmed time function based on experimental data. The downstream side is bounded by a choked thrust nozzle. The flow through the turbine-bleed line is assumed negligible compared with the choked-thrust-nozzle flow. A block diagram of the simplified system is shown in figure 4.

Two engine systems were studied, one with an axial pump, and the other with a radial pump. For each system a controlled experimental test was conducted in which step-like disturbances were programmed in pump speed. The resulting response in pump-inlet

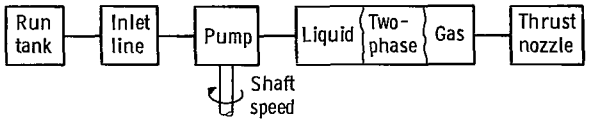

Figure 4. - Simplified system.

flow is shown for the axial-pump system in figure 5(a) and for the radial-pump system in figure 5(b). For the axial-pump system the speed steps occurred every 2.0 seconds, with the initial step at about $t = 16.0$ seconds. The initial speed step for the radial-pump system occurred at about $t = 10.5$ seconds, with the subsequent steps spaced every 3.0 seconds.

In general, the initial flow responses are the most oscillatory. And as time increases, the flow responses become more damped. It will be shown that this transition to a more damped response is due to three major factors: (1) the pump operating point, (2) the amount of two-phase fluid in the system, and (3) the general cooldown of the system material, with the subsequent lower temperature gas powering the turbine.

To study this phenomenon, three specific flow responses are simulated. Two are for the axial-pump system and one is for the radial-pump system. The axial-pump system simulations, are of (1) the most oscillatory response, from $t = 15.9$ to 18.2 seconds, and (2) the more damped response from $t = 22.2$ to 24.2 seconds. Thus, the transition to a more damped response can be studied. Then by simulating the radial-pump system response (fig. 5(b)) from $t = 13.5$ to 15.8 seconds, the generality of this phenomenon between engine systems is established.

There are two flow responses not simulated for the axial-pump system between $t = 18.2$ and $t = 22.2$ seconds, as illustrated in figure 5(a). During these responses the pump operated both in-stall and out-of-stall. There is some uncertainty about the mechanisms involved during the transition into and out of stall. It was decided not to introduce this uncertainty into the simulation. Hence, the first time period during which the pump operated completely out-of-stall ($t = 22.2$ to 24.2 sec) was selected.

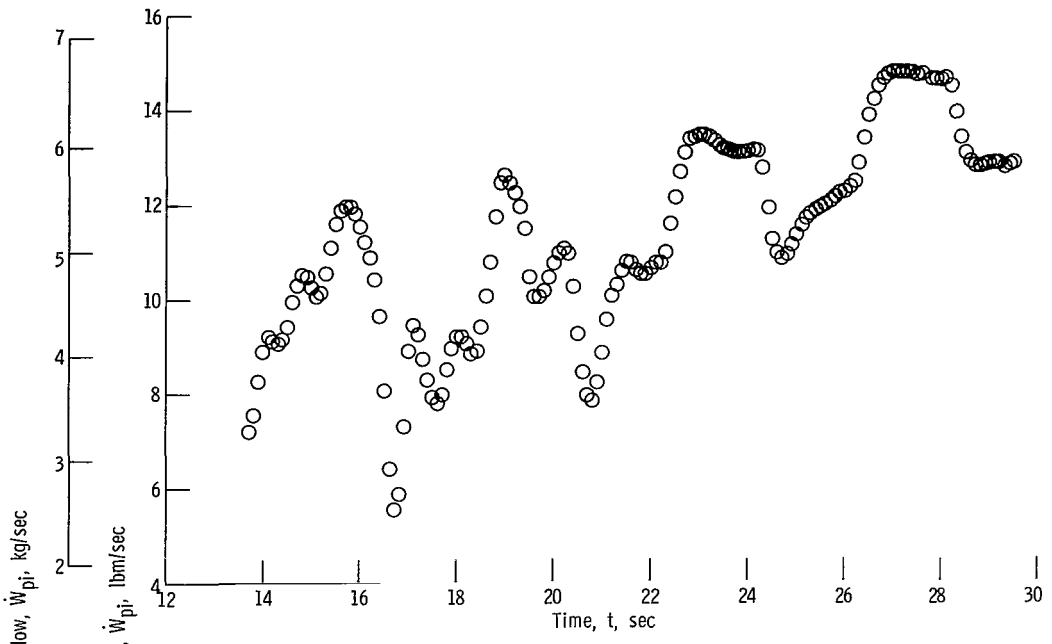

(a) Axial-pump system.

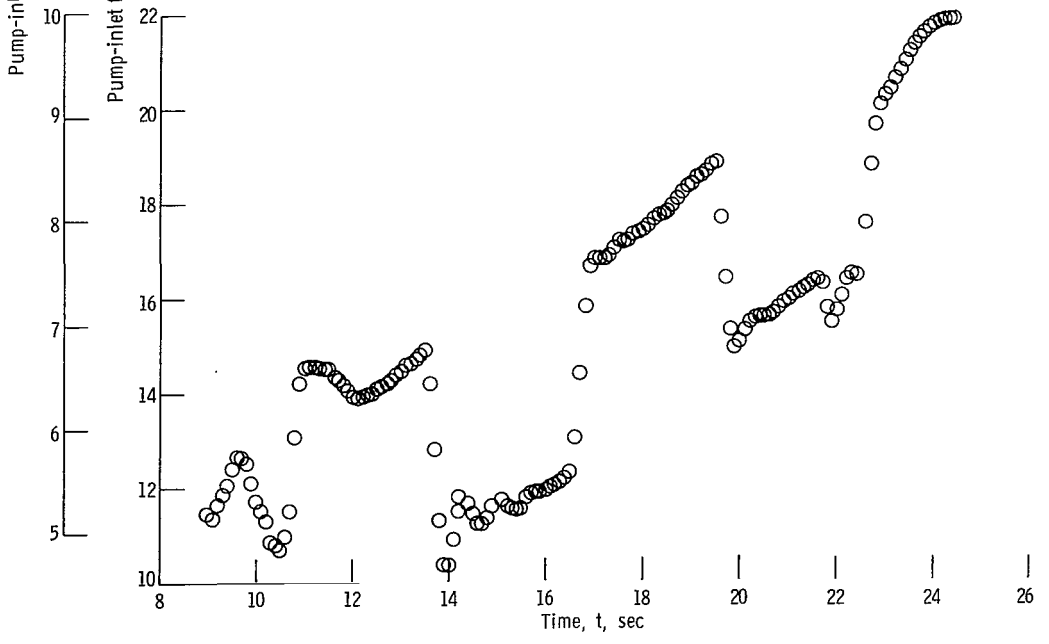

(b) Radial-pump system.

Figure 5. - Pump-inlet flow transients resulting from controlled, step-like, pump speed disturbance in experimental test.

During the three simulated time periods, the two-phase fluid was located in approximately the same section of the system. The saturated-liquid fluid boundary was inside the nozzle-coolant tubes and the saturated-gas fluid boundary was just inside the reflector. This choice of time periods, therefore, also simplified the computer model. The high-speed repetitive-operation portion of the analog, which locates the moving fluid boundaries, need only consider the system from the nozzle-inlet manifold to the reflector exit. The result is a large reduction in necessary analog computing equipment.

In the remainder of the report the two nuclear-rocket cold-flow engine systems will be briefly described. The analog computer model will be presented, with a discussion on mass-flow storage and with most equation derivations referred to appendixes A to E. The analytical data from the system response simulations of the three time periods of interest will then be discussed and compared with experimental values.

DESCRIPTION OF NUCLEAR-ROCKET ENGINE SYSTEMS

The Axial-Pump System

The nuclear-rocket cold-flow test facility was located at the Plum Brook Station of the Lewis Research Center. The altitude exhaust system (fig. 1) maintained a rocket-nozzle-exhaust pressure of approximately 0.5 psia (3450 N/m^2). The rocket engine was mounted in the structure at the top right in the figure in a down-firing position.

A schematic diagram of the rocket-engine test package using the axial pump is also shown in figure 1. The test hardware consisted of a turbopump assembly, unfueled reactor, and a supersonic exhaust nozzle. The liquid-hydrogen run tank which fed the pump, had a servocontrolled pressurizing system. An 8-inch (0.2-m) diameter line, which was equipped with a turbine flowmeter, connected the pump to the run tank.

The turbopump assembly consisted of a Rocketdyne MARK-IX turbopump, turbine-power-control valve, and turbine-bleed line The liquid-hydrogen pump was composed of an axial-entrance mixed-flow axial-discharge inducer stage, six identical high-pressure axial-flow stages, and a single-outlet collecting volute. The turbine was a six-stage pressure-compounded axial-flow unit designed for operation with hot or ambient temperature gaseous hydrogen.

The pump discharged into a 4-inch (0.1-m) diameter stainless steel flight-weight feedline equipped with a servocontrolled butterfly valve used for flow control. Approximately 18 feet (5.5 m) downstream from the main flow-control valve, the propellant line divided equally into three smaller ducts that fed the nozzle-inlet manifold.

The regeneratively cooled (with liquid hydrogen) tubular-wall nozzle utilized single-pass cooling. The liquid hydrogen entered the tubes through three equally spaced inlet connections on the manifold and flowed toward the reactor end.

On discharging from the nozzle-coolant tubes, the fluid entered the reflector-inlet-manifold section of the reactor assembly. From there it passed through the reflector component that was composed of an inner graphite reflector, an outer aluminum reflector, simulated aluminum control rods, and the aluminum pressure vessel. The fluid then entered the reactor core, flowing through the many parallel coolant passages in the unloaded graphite reactor core.

The warm hydrogen emerged from the core into the nozzle thrust chamber where most of it was exhausted into the facility vacuum exhaust. A small portion of the fluid, however, was bled to the turbine through a 3-inch (0.076-m) diameter bleed port, the turbine-bleed line, and the servocontrolled turbine-power-control valve. Altogether, the rocket-engine system tested was a full-scale model of what might have been a flight version of a system using the Kiwi reactor.

The Radial-Pump System

This nuclear-rocket cold-flow test facility was also located at the Plum Brook Station. Except for a few specific changes, this test facility (ref. 2) was assembled identically as the test facility for the axial-pump system (fig. 1).

The turbopump was changed to an Aerojet Mark III, Mod 4 turbopump. The liquid-hydrogen pump was a radial flow, centrifugal type with an integral three-blade helical inducer. The turbine was a two-stage pressure-compounded impulse type.

The only other change was in the propellant ducting. The inlet piping that connected the pump to the run tank was lengthened by about 6 feet (1.8 m).

AN ANALOG COMPUTER PROGRAM FOR SIMPLIFIED ENGINE SYSTEMS

An analog computer program is developed for the nuclear-rocket cold-flow engine systems described in the previous section. The purpose of this program is to study system transient response to step-like, pump-speed disturbances. Experimental data are utilized in several areas of the analog model to simplify the program and help to establish the operating levels of pressure and temperature observed in the experimental tests. Emphasis is placed on analyzing the frequency and damping content of the computer results, rather than on how well the experimental data are reproduced.

Principles of Operation

The simplified representation for the systems simulation is shown in figure 6. Experimental data are utilized for the pump speed and for the nozzle-inlet-manifold fluid enthalpy. The pump-speed forcing function, combined with neglecting turbine-bleed line flow, eliminates the need to simulate the turbine-bleed line, servocontrolled turbine-power-control valve, and turbine. The enthalpy forcing function defines a reference point in a section of the analog program called the spatial-distribution model. This, as demonstrated in appendix E, further simplifies the computer representation.

The analog computer program consists of two parts: (1) a slow-speed analog, and (2) a high-speed analog. With the exception of the spatial-distribution model, the entire system in figure 6 is programmed on the slow-speed analog. The spatial-distribution model is solved on the high-speed analog.

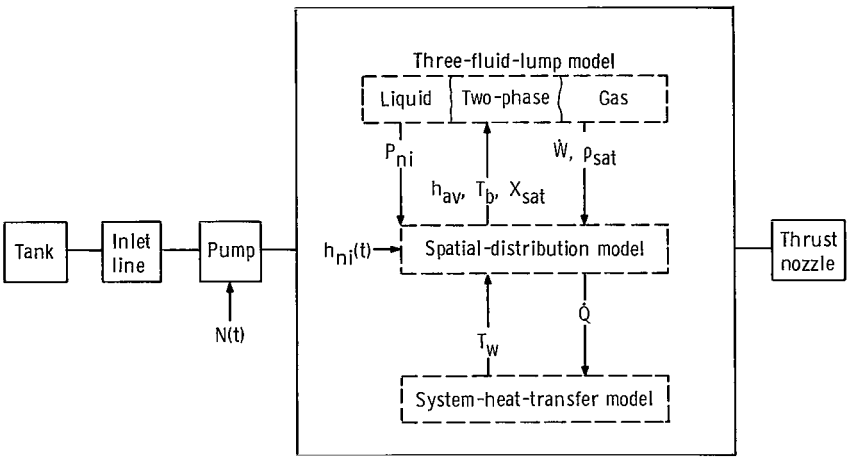

Figure 6. - Simplified system for analog computer program.

The slow-speed analog is operated at 1/100 real time; that is, 100 seconds of computer operation are required to generate one second of solution. The high-speed analog is operated repetitively at 5 hertz relative to slow-speed analog operation. It follows from these two rates that the spatial-distribution model updates its outputs 500 times per second of solution.

The high-speed analog solution is assumed to take place fast enough such that the input variables from the slow-speed analog appear as constants. Spatial distributions are computed with the aid of high-speed integration with distance x as the independent variable. Certain variables (see appendix D) are then sampled, stored, and then sent

as updated inputs to the slow-speed analog. The high-speed analog is then reset and the computation restarted with new inputs from the slow-speed analog.

Model Lumping

A diagram of the model lumping was presented in figure 6. The first lump to be considered is the run tank. For each engine system, the run tank is treated as a constant-pressure liquid-hydrogen supply.

The all-liquid pump-inlet line is a stationary, constant-geometry lump. It is assumed that the walls of the inlet line have lost all of their latent heat content during a pretest cooldown. Hence, the operation of this lump is based on the conservation of fluid mass and momentum principles. Fluid energy considerations are neglected.

A normalized, steady-state pump characteristic is used to represent the pump. A comparison of the operating characteristics of the two types of pumps is shown in figure 7.

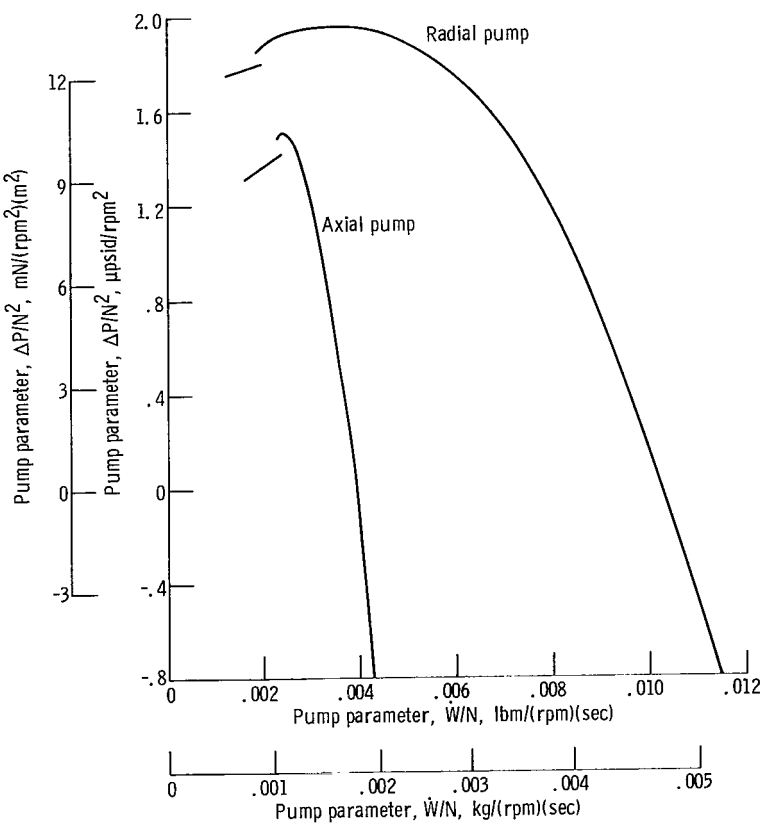

Figure 7. - Operating characteristics of pumps used in axial- and radial-pump systems.

The data for the radial-pump operating characteristic was obtained from a series of special pump tests. However, the axial-pump operating characteristic was derived with quasi-steady-state data points from the series of tests conducted.

Consider the portion of the system in figure 6 between the pump and the thrust nozzle. The mathematical model for this section consists of three parts: (1) the three-fluid-lump model, (2) the spatial-distribution model, and (3) the system-heat-transfer model. Arrows are drawn in the figure to illustrate the general flow of information between the three parts. The fundamental principle in the operation of this model concerns the storage of mass flow in the system. It is shown in appendix A that the amount of storage is proportional to the thermodynamic fluid property $[\partial\rho/\partial P]_h$ and, further, that most of the storage takes place in the two-phase fluid near the saturated-liquid boundary.

The three-fluid-lump model consists of three variable, special lumps called fluid-lumps: a liquid lump, a two-phase lump, and a gas lump. The two-phase fluid is treated as a homogeneous mixture; the state equation used is derived in appendix B. The operation of this three-fluid-lump model is based on the conservation of fluid mass and momentum principles.

The primary function of the spatial-distribution model is to maintain the conservation of fluid energy. The operation of this lump is characterized by high-speed, repetitive generation of the x-distributions of certain variables. The x-distribution of the fluid property $[\partial\rho/\partial P]_h$, for instance, is calculated and averaged every cycle. This, in turn, provides for approximating the amount of mass-flow storage in a fluid-lump (appendix A).

The system-heat-transfer model consists of several stationary lumps, each representing a fixed amount of system mass. The operation of this part is based on the conservation of energy as applied to the system material. As a result, approximate cool-down rates are determined for different sections of the system.

The combined operation of the three-fluid-lump, the spatial-distribution, and the system-heat-transfer models fully represents the section of the engine systems between the pump and the thrust nozzle. In summary, the main fluid-dynamic calculations are performed by the three-fluid-lump model, with the system-heat-transfer model supplying the more slowly varying heat-transfer dynamics. The spatial-distribution model performs high-speed averaging and x-distribution calculations.

The thrust nozzle represents the final lump (fig. 6) to be considered. The nozzle is assumed choked at all times. The thrust-nozzle-chamber pressure calculation is based on the conservation of fluid mass between the core exit and the nozzle exhaust. The turbine-bleed-line flow is neglected. Neglecting energy considerations, the core-exit fluid temperature is used in the thrust-nozzle chamber.

The basic mathematical equations programmed on the analog computer are derived in appendixes A, B, and C. Specific equations are developed for each lump in appendixes D and E.

DISCUSSION OF RESULTS

The analytical data presented in this section are the results of dynamics studies using a simplified model for the engine systems. Experimental data were programmed into those areas which would add unnecessary complexity to the model and have a negligible effect on the low-frequency dynamics under study. The emphasis of the following discussion, therefore, shall be mainly on the frequency and damping content of the computer data, rather than on how well the experimental data are reproduced.

Input Forcing Functions

Pump-speed forcing functions. - The pump-speed forcing functions used are illustrated in figure 8. The curves show the response of the pump to step-function speed demands initiated in the turbine-power-control valve control system. The control-system function was to rapidly accelerate or decelerate the pump speed between 4500 and 5500 rpm to the demanded speed.

The speed curve in figure 8(a) shows the response in the axial-pump system to a down-speed step demand. The demand, initiated at $t = 16.3$ seconds, called for a deceleration from 5500 to 4500 rpm. The preceding 0.4 second is included in the forcing function, however, to establish a low flow acceleration starting point. To minimize computation starting transients, it is desirable to begin a computer solution at a steady-, or at least a quasi-steady-, state point. During the 0.4 second from $t = 15.9$ to 16.3 seconds the turbine-power-control valve control system was decelerating the pump speed toward 5500 rpm to compensate for the approximately 350-rpm overshoot existing at $t = 15.9$ seconds.

The speed curve for the second time period considered in the axial-pump system is presented in figure 8(b). The speed demand initiated at $t = 22.2$ seconds called for an acceleration from 4500 to 5500 rpm. At this time in the test, however, the lower-energy turbine-inlet gas was unable to accelerate the turbine sufficiently to satisfy the demand. Consequently, as shown in figure 8(b), the speed response fell short to the demanded 5500 rpm and, further, the turbine-power-control system was unable to maintain a steady final value of pump speed. This more sluggish system response has an appreciable effect on the subsequent flow dynamics, as will become evident later.

The speed curve in figure 8(c) shows the response in the radial-pump system to a step demand. The demand, calling for a deceleration from about 5500 to 4500 rpm, was initiated at $t = 13.5$ seconds. The resulting speed response was similar to the axial-pump system response shown in figure 8(a). The radial-pump system response, however, has a small oscillation superimposed on the general deceleration waveform. This more oscillatory system response is also apparent in the resulting low-frequency flow dynamics,

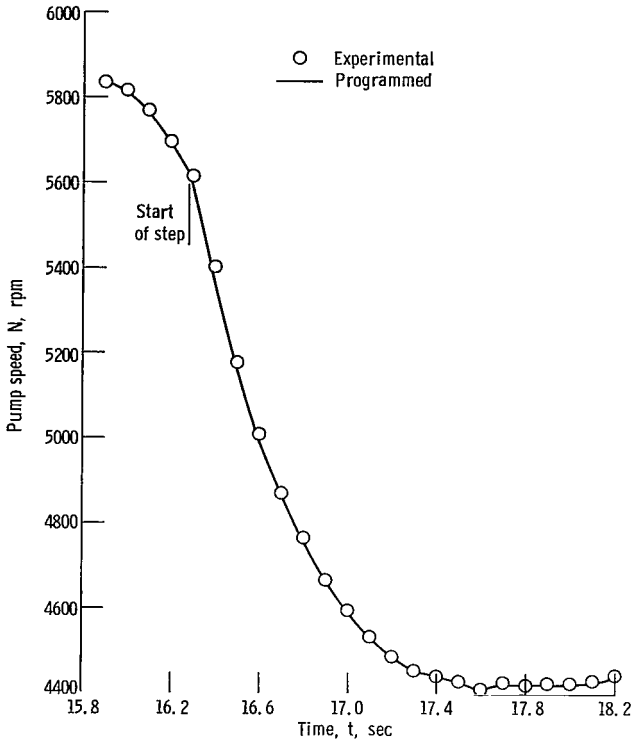

(a) For axial-pump system time period beginning at t = 15.9 seconds.

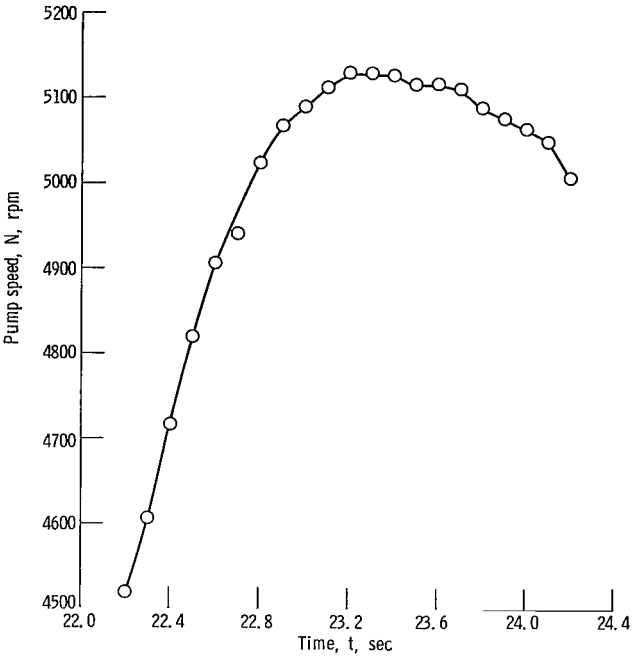

(b) For axial-pump system time period beginning at t = 22.2 seconds.

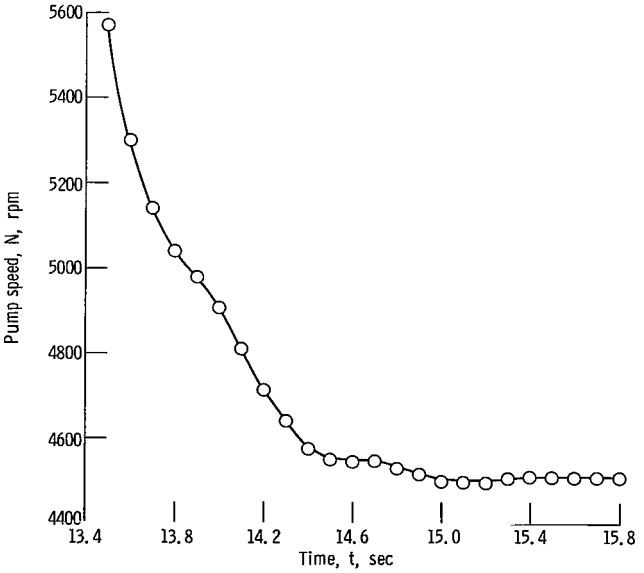

(c) For radial-pump system time period.

Figure 8. - Programmed pump-speed forcing functions.

as will be demonstrated later.

Nozzle-inlet-manifold fluid-enthalpy forcing functions. - The curves shown in figure 9 are the forcing functions used for the nozzle-inlet-manifold fluid enthalpy h_{ni}. The experimental data points were calculated from measured values of fluid temperature and pressure. The liquid-hydrogen-properties digital subroutine (presented in ref. 3) was used.

The solid line in each figure represents a linear least-squares curve fit of the experimental data points. The dotted line is an approximate saturated-liquid-enthalpy reference line and is determined by the nozzle-inlet-manifold pressure. The vertical distance that the solid line is below the dotted curve indicates the degree of fluid subcooling. Two-phase fluid exists whenever the solid line is above the dashed reference curve.

The use of a h_{ni} forcing function establishes a reference point in the system near the saturated-liquid fluid boundary. This eliminates the need for fluid and material energy equations to predict the fluid enthalpy spatial distribution for the upstream, low-heat-content portion of the systems. The result is a significant reduction in the amount of necessary analog computing equipment.

The enthalpy curves in figure 9(a) are for the axial-pump time period beginning at $t = 15.9$ seconds. Two-phase fluid exists in the nozzle-inlet manifold from $t = 16.8$ to 17.7 seconds. No experimental data points are presented for these times since fluid temperature and pressure do not define a unique value of two-phase fluid enthalpy. Relative to the curves in figures 9(b) and (c), the fluid enthalpy in this figure shows the least amount of subcooling. As will be shown later, the amount of fluid subcooling in the nozzle-inlet manifold significantly affects the low-frequency flow dynamics, since it is a major factor in determining the amount of two-phase fluid in the system.

The largest amount of fluid subcooling is indicated by the enthalpy curves in figure 9(b). These curves are also for the axial-pump system, but for the later time period beginning at $t = 22.2$ seconds. At this point in the test, the rate of heat addition to the hydrogen from the cooled, upstream system material was low. This is illustrated by the small time rate of change of the h_{ni} curve.

The enthalpy curves in figure 9(c) are for the radial-pump time period beginning at $t = 13.5$ seconds. The significant amount of fluid subcooling is similar to that shown in figure 9(b). As indicated by the relatively large time rate of change of the h_{ni} curve, the upstream system material was rapidly cooling off during this period of the test.

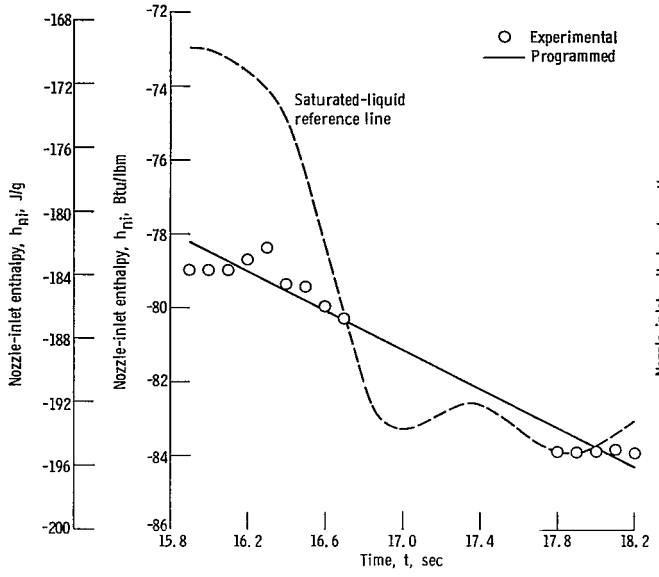

(a) For axial-pump system time period beginning at t = 15.9 seconds.

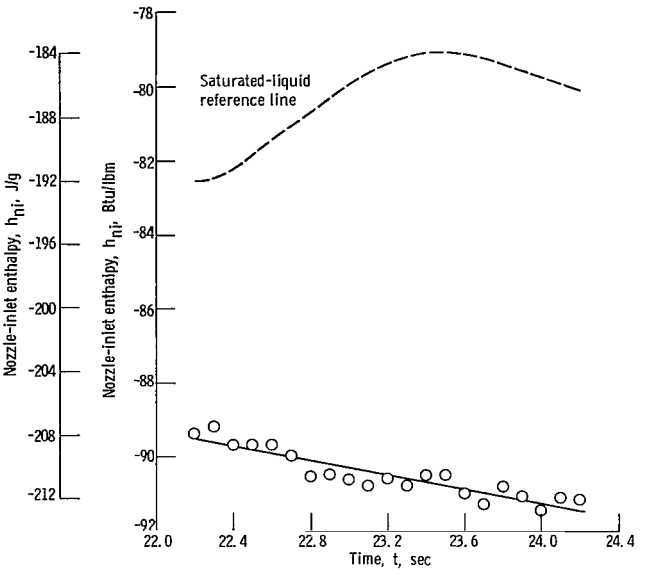

(b) For axial-pump system time period beginning at t = 22.2 seconds.

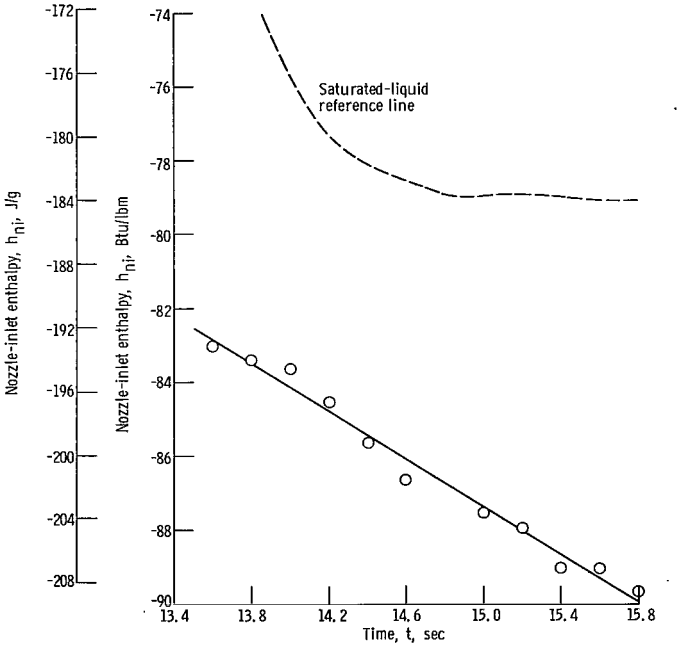

(c) For radial-pump system time period.

Figure 9. - Programmed nozzle-inlet-manifold fluid enthalpy forcing function.

Comparison of Predicted and Measured Data

In general, the predicted fluid flow, pressure, and temperature data are within ±13 percent of the measured values, as illustrated by figures 10 to 14. The predicted values are identified in the figures with solid lines, and the experimental measurements are identified with symbols.

The predicted and measured values for pump-inlet flow are compared in figure 10. In figure 11, the predicted and calculated data for the thrust-nozzle-chamber flow are compared. The experimental thrust-nozzle-chamber flow is calculated with a choked-nozzle equation (appendix E) from experimental measurements of thrust-nozzle-chamber fluid temperature and pressure. The pump-inlet and thrust-nozzle-chamber flows together show that the proper mass-flow storage in the system has been approximated.

The frequency and damping content of the predicted pump-inlet flow agree reasonably well with observation. The predicted period of oscillation for the solution beginning at $t = 15.9$ seconds in figure 10(a) shows good agreement, except for a slight time shift of approximately 0.1 second. The largest error in the flow period is shown in figure 10(b) during the initial portion of the transient. Discounting the approximate 0.1-second time shift, the period is off by about 13 percent at $t = 14.3$ seconds.

Figure 12 shows the pump-inlet and pump-outlet pressures. The predicted values of nozzle-inlet-manifold pressure and the thrust-nozzle-chamber pressure are compared with the experimental values in figure 13. In general, the calculated pressure levels compare well with observation. The pressure rise between the pump outlet and inlet (fig. 12) is governed by the pump operating characteristics. The nozzle-inlet-manifold pressure (fig. 13) is an initial condition for the spatial-distribution model solutions and is approximated with a simplified equation (appendix D).

The predicted thrust-nozzle-chamber fluid temperature is compared with an experimental average value in figure 14. For the axial-pump system the experimental temperature represents an arithmetic average of the five available measured values. The experimental temperature for the radial-pump system, however, involves additional measured values, plus a weighting technique to account for the cross-sectional distribution of temperature. In general, the results are close to observation, considering the single-lump treatment of the entire gas phase.

The two metal temperatures generated in the computer model are shown in figures 15 and 16. The temperature $T_{w,ns}$ is an average value for the nozzle-coolant-tubes shell material and is presented in figure 15. The indicated experimental values are measured about midway along the shell length. As shown, the predicted cooldown of this material agrees very well with experimental data.

The metal temperature $T_{w,ri\text{-}ce}$ (fig. 16) is an average value for the entire gas fluid-lump. The experimental values shown were measured at six designated points be-

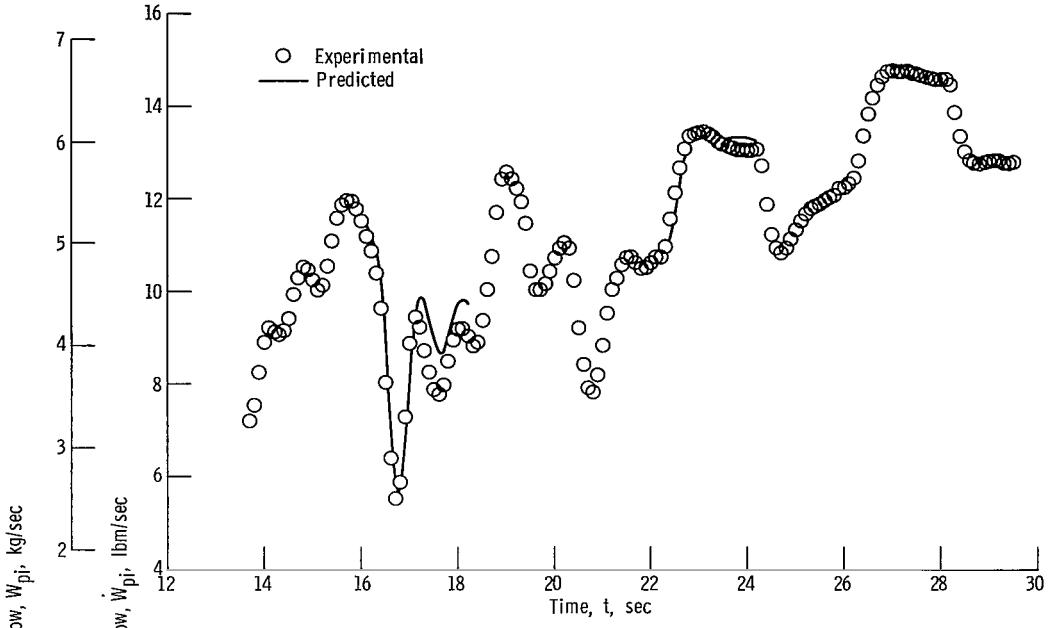

(a) For axial-pump system time periods.

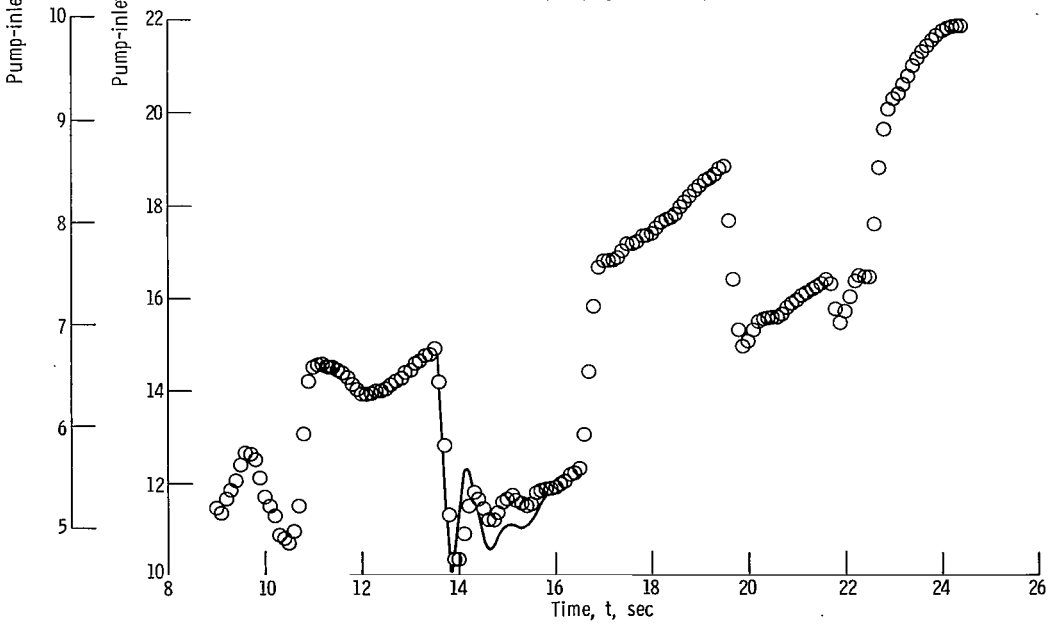

(b) For radial-pump system time period.

Figure 10. - Pump-inlet flow.

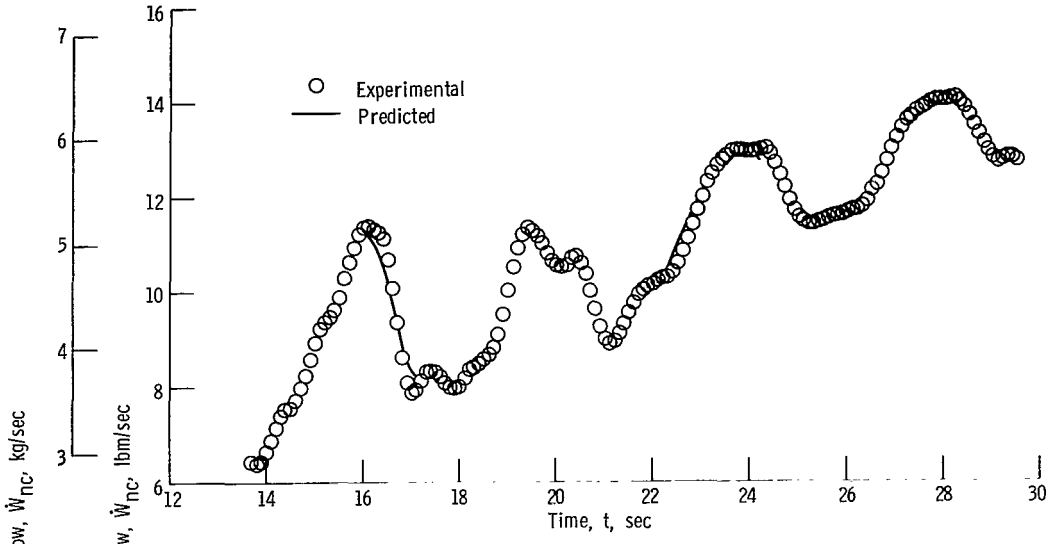

(a) For axial-pump system time periods.

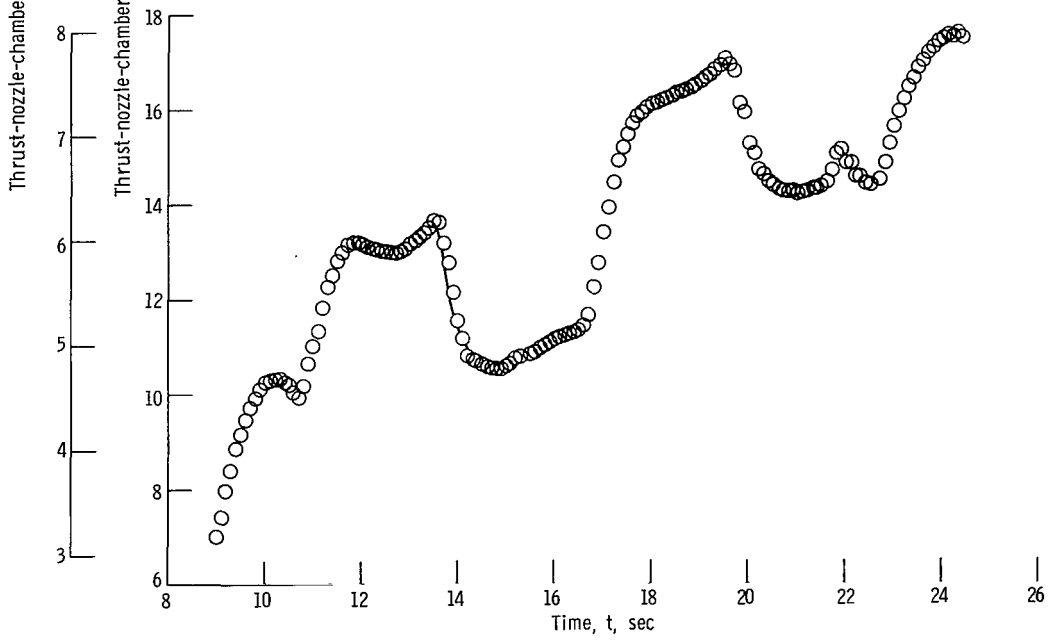

(b) For radial-pump system time period.

Figure 11. - Thrust-nozzle-chamber flow.

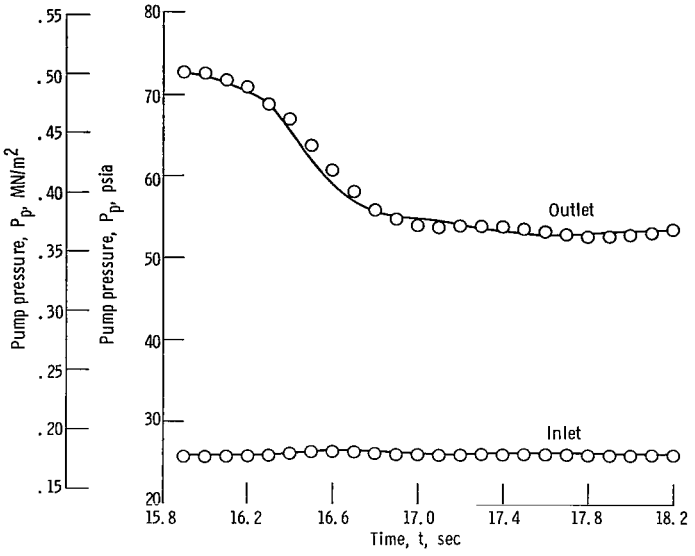

(a) For axial-pump system time period beginning at t = 15.9 seconds.

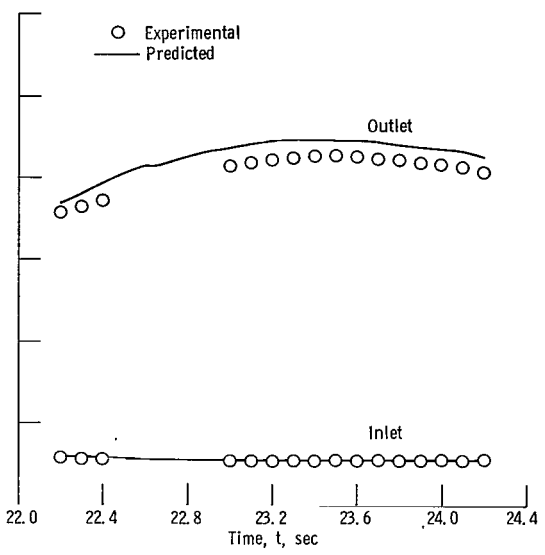

(b) For axial-pump system time period beginning at t = 22.2 seconds.

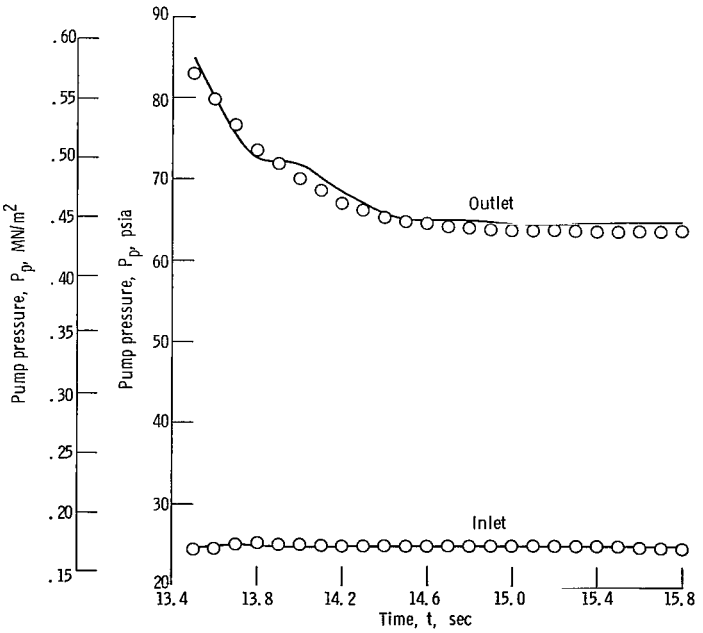

(c) For radial-pump system time period.

Figure 12. - Pump-inlet and pump-outlet pressures.

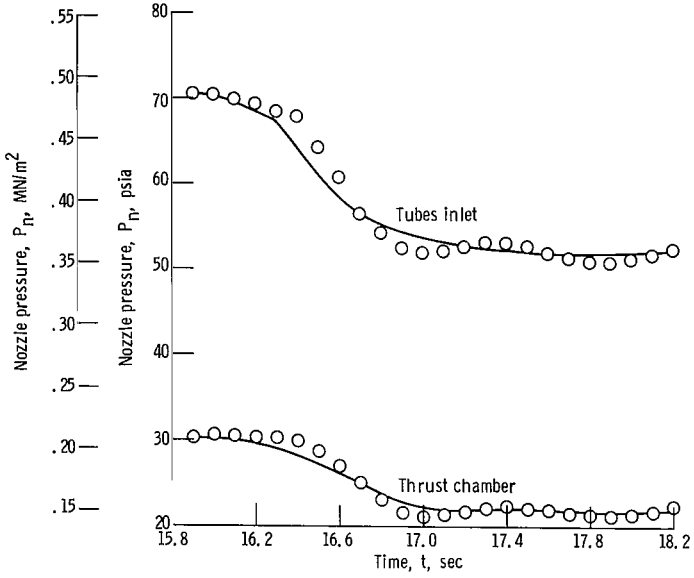

(a) For axial-pump system time period beginning at t = 15.9 seconds.

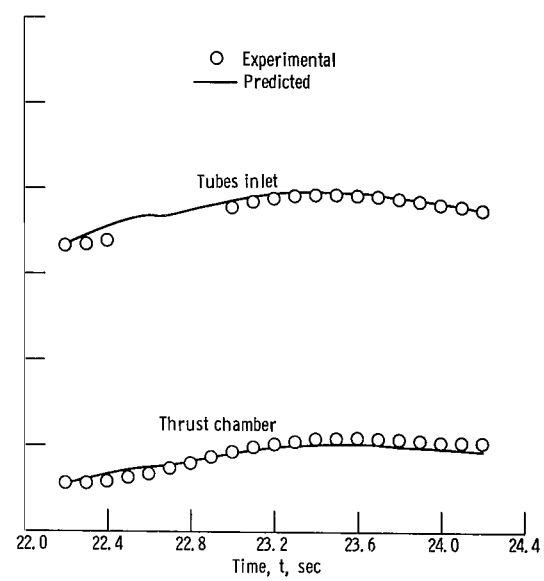

(b) For axial-pump system time period beginning at 22.2 seconds.

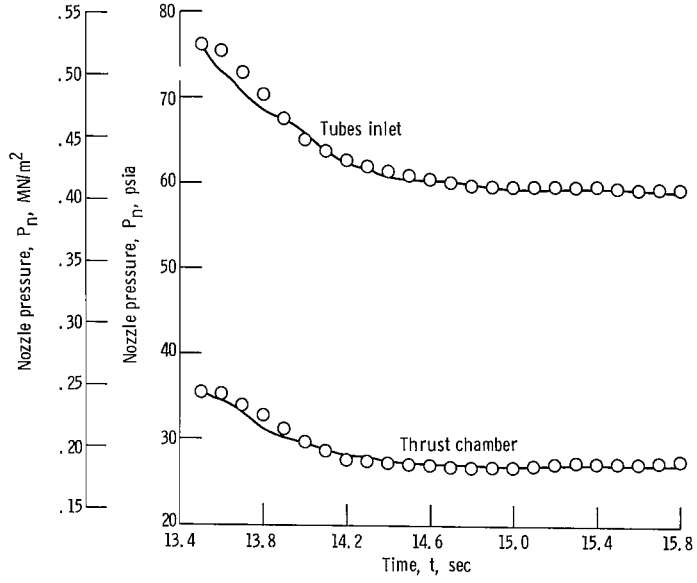

(c) For radial-pump system time period.

Figure 13. - Nozzle-inlet-manifold and thrust-nozzle-chamber pressures.

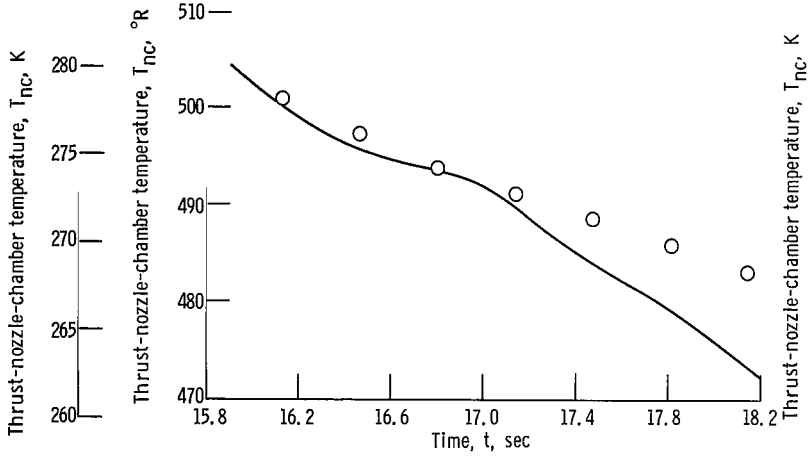

(a) For axial-pump system time period beginning at t = 15.9 seconds.

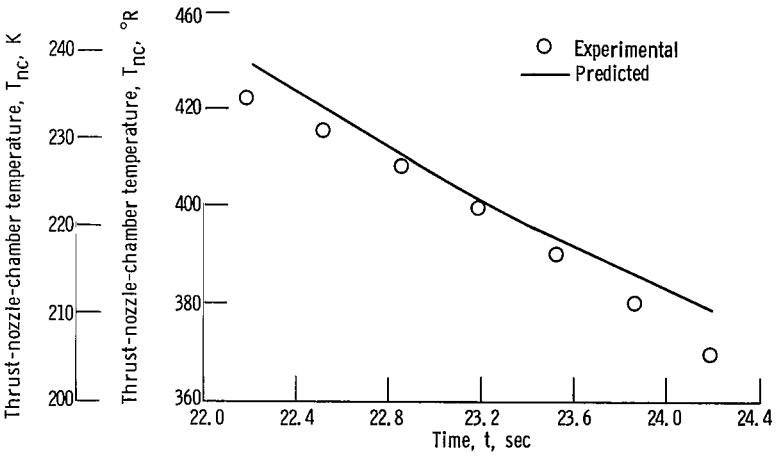

(b) For axial-pump system time period beginning at t = 22.2 seconds.

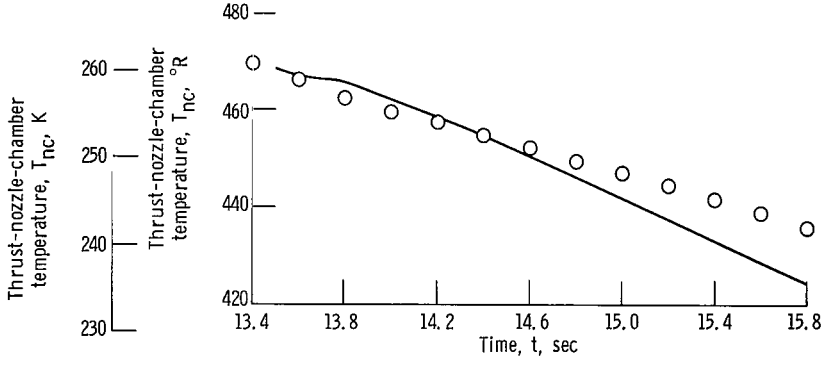

(c) For radial-pump system time period.

Figure 14. - Thrust-nozzle-chamber fluid temperature.

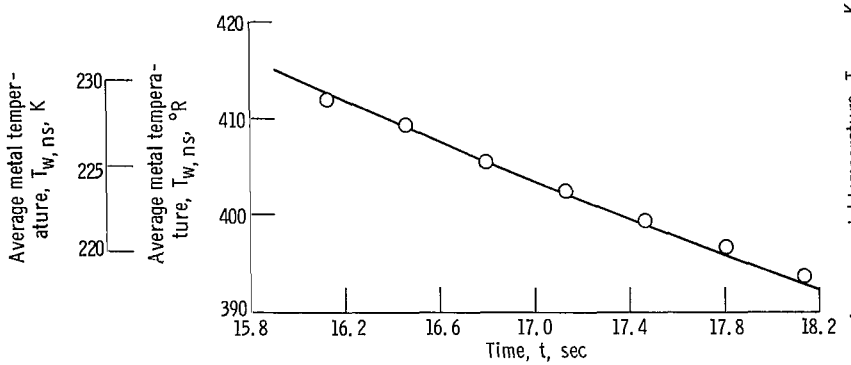

(a) For axial-pump system time period beginning at t = 15.9 seconds.

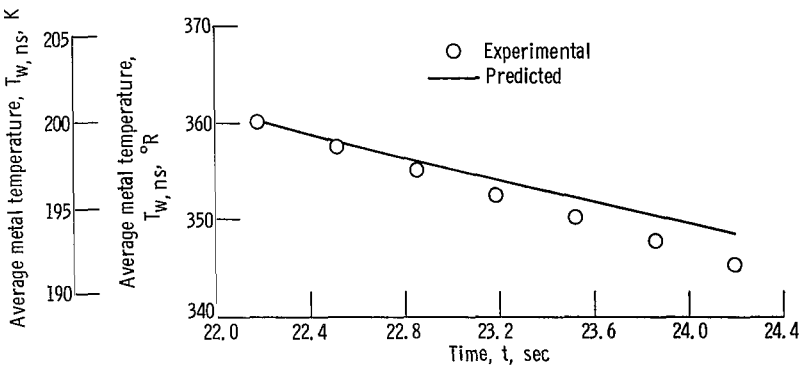

(b) For axial-pump system time period beginning at t = 22.2 seconds.

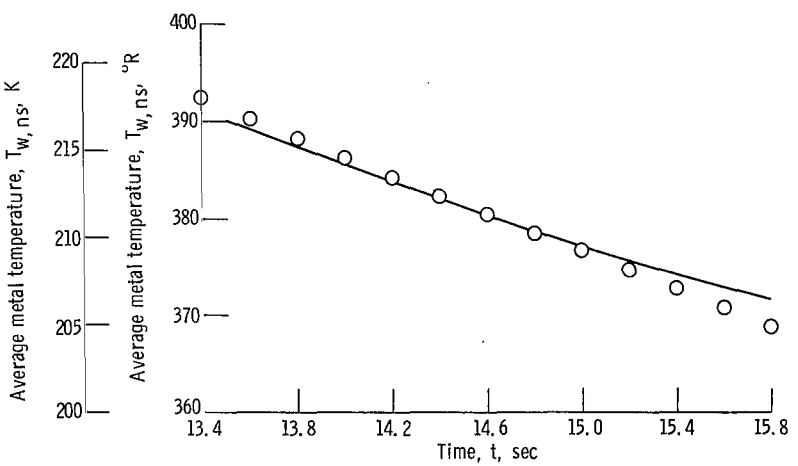

(c) For radial-pump system time period.

Figure 15. - Nozzle-coolant-tubes shell average metal temperature.

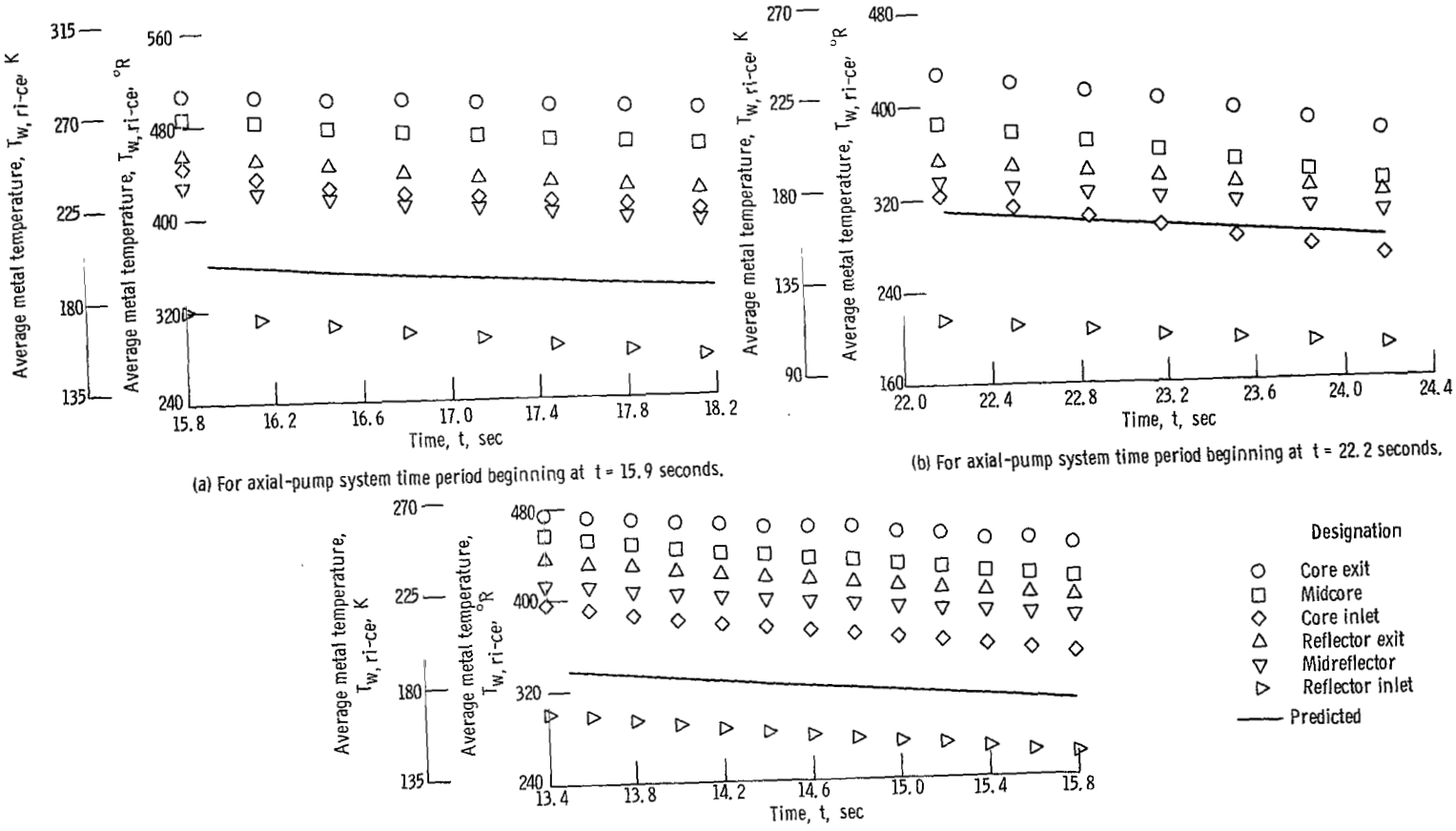

(a) For axial-pump system time period beginning at t = 15.9 seconds.

(b) For axial-pump system time period beginning at t = 22.2 seconds.

(c) For radial-pump system time period.

Figure 16. - Reflector-inlet-to-core-exit average metal temperature.

tween the reflector inlet and the core exit. In general, the predicted values are low. However, the slopes of the curves indicate that the observed cooldown rates have been approximately duplicated. Hence the total input heat flux to the gas fluid-lump $\dot{Q}_g$ has been approximated. The value of $\dot{Q}_g$, in turn, is used to calculate the core-exit fluid temperature (fig. 14). The equations (pp. 62 and 73, appendix D), which demonstrate this effect are as follows:

$$\frac{\partial T_{w,ri\text{-}ce}}{\partial t} = -\frac{\dot{Q}_g}{M_{ri\text{-}ce} c_{p,sg\text{-}ce}}$$

$$T_{b,ce} = T_{sat} + \frac{\dot{Q}_g}{\dot{W}_g c_{p,g}}$$

(Symbols are defined in appendix F.)

Predicted Movements of Fluid Boundaries

The curves of figure 17 represent the calculated movements of the saturated-liquid and the saturated-gas fluid boundaries. The values plotted correspond to the respective distances of the fluid boundaries measured downstream from the nozzle-inlet manifold. No experimental measurements, unfortunately, are available for comparison. However, a few qualitative comments may be made.

In general, the saturated-gas fluid boundary moves less than the saturated-liquid fluid boundary. This downstream fluid boundary is situated inside the high-input - heat-flux reflector throughout all of the computer solutions. Thus, only a small spatial shift of the boundary is required to compensate for an impinging flow disturbance. The effect is exemplified in the axial-pump system simulation by comparing the boundary movements computed during the two speed disturbances (figs. 17(a) and (b)). The largest movement is observed during the second disturbance, after the reflector material has cooled to a lower temperature.

The nozzle-coolant-tubes region upstream of the throat is a low-input - heat-flux region, and the remaining portion of tubes downstream is a relatively high-input - heat-flux region, as illustrated in figure 18. Accordingly, the most significant spatial movements of the saturated-liquid fluid boundary takes place upstream of the throat, as shown in figure 17. The time rate of change of the boundary position clearly decreases (fig. 17(b)) as the boundary shifts downstream of the throat.

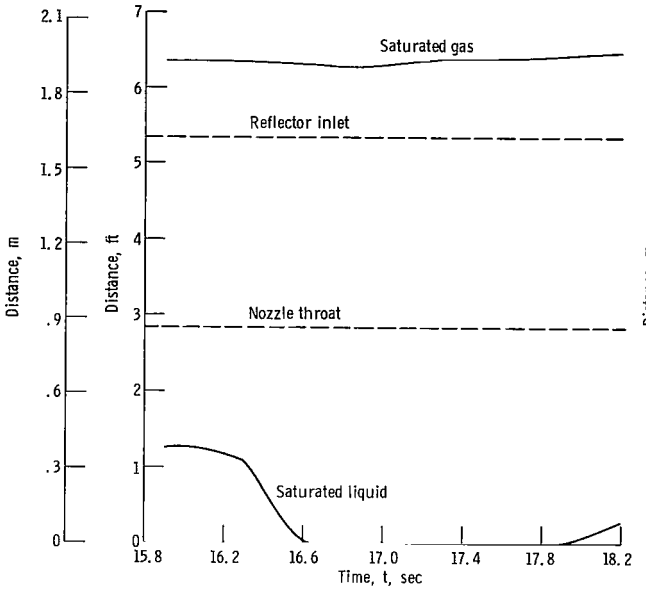

(a) For axial-pump system time period beginning at t = 15.9 seconds.

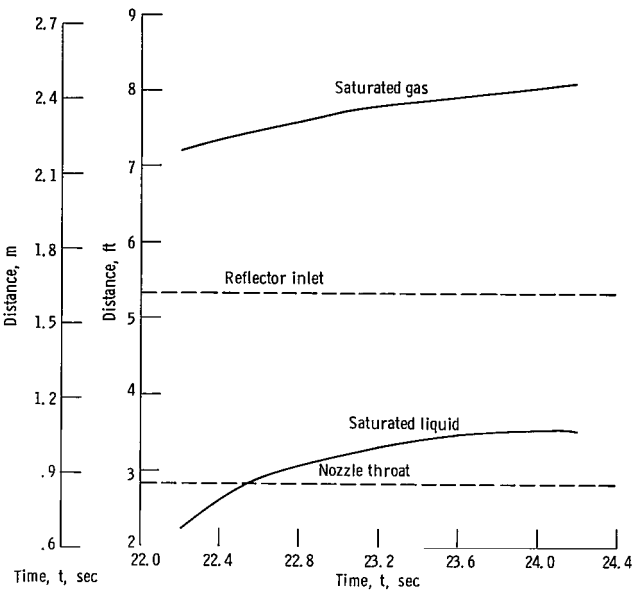

(b) For axial-pump system period beginning at t = 22.2 seconds.

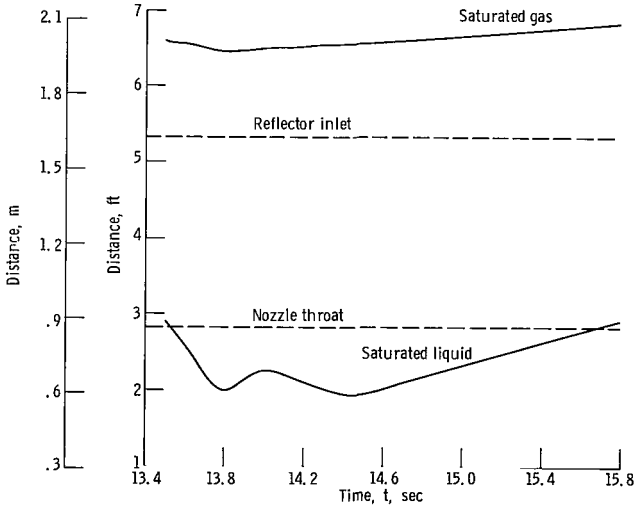

(c) For radial-pump system time period.

Figure 17. - Predicted distance downstream of nozzle-inlet-manifold of two-phase saturated fluid boundaries.

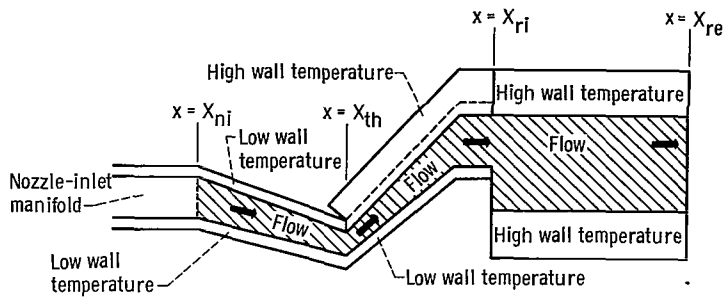

Figure 18. - Simplified diagram of nozzle-inlet-manifold-to-reflector-exit region showing areas of high and low wall temperatures.

Effect of the Pump Characteristics

Operation on positively sloped segments of the normalized pump characteristics (see fig. 7) will reduce the damping of flow transients. In fact, it is concluded in reference 4 that overall system instability will occur if the pump-map slope exceeds a certain critical, positive value. To demonstrate the sensitivity of the pump-map slope and the tendancy of positive slopes to counteract friction losses, parametric studies for the two engine systems will be presented. The resulting curves, therefore, are parametric solutions and not actual system transients.

Axial-pump system. - The pump operates in stall (positive slopes) during the entire solution beginning at $t = 15.9$ seconds and operates out-of-stall (negative slopes) during the solution beginning at $t = 22.2$ seconds. An approximate steady-state pump map was derived for the out-of-stall region using data from 10 experimental tests. No steady-state data points were found for the stall region, however. Consequently, normal operation in-stall is assumed to take place on a constant, positively sloped characteristic. A value for the stall slope was selected which yielded solutions in good agreement with experimental data.

Six constant-slope variations of the pump characteristic are assumed. The three in-stall variations and the three out-of-stall variations are shown in figure 19. A portion of the negatively sloped, out-of-stall pump map is included also as a dotted line. For each set of three variations considered, the solution is begun at the same initial conditions, and the subsequent pump operation is defined by the constant-slope variations.

The curves in figure 20 represent the solutions for pump-inlet flow, which result from the parametric variation of the pump-map slope. The flows resulting from the in-stall variations are shown in figure 20(a), and the out-of-stall curves are shown in figure 20(b). Comparing the in-stall and out-of-stall solutions thus establishes the high sensitivity of the system response to a positive pump-map slope. And further, the de-

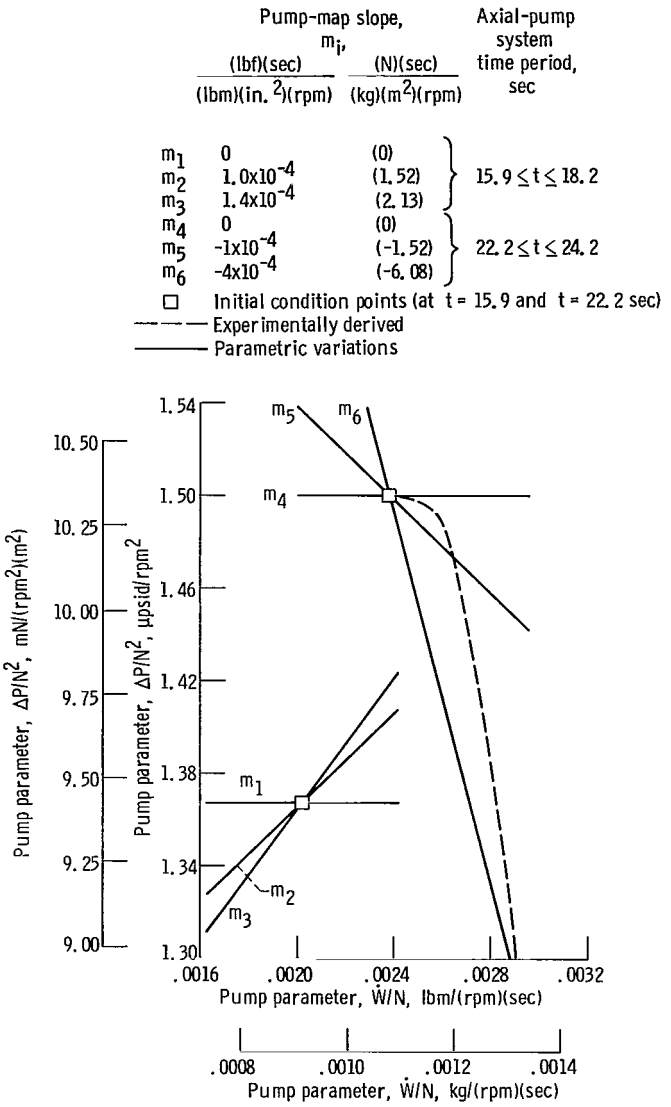

Figure 19. - In-stall and out-of-stall pump-map slope variations considered for axial-pump system time periods.

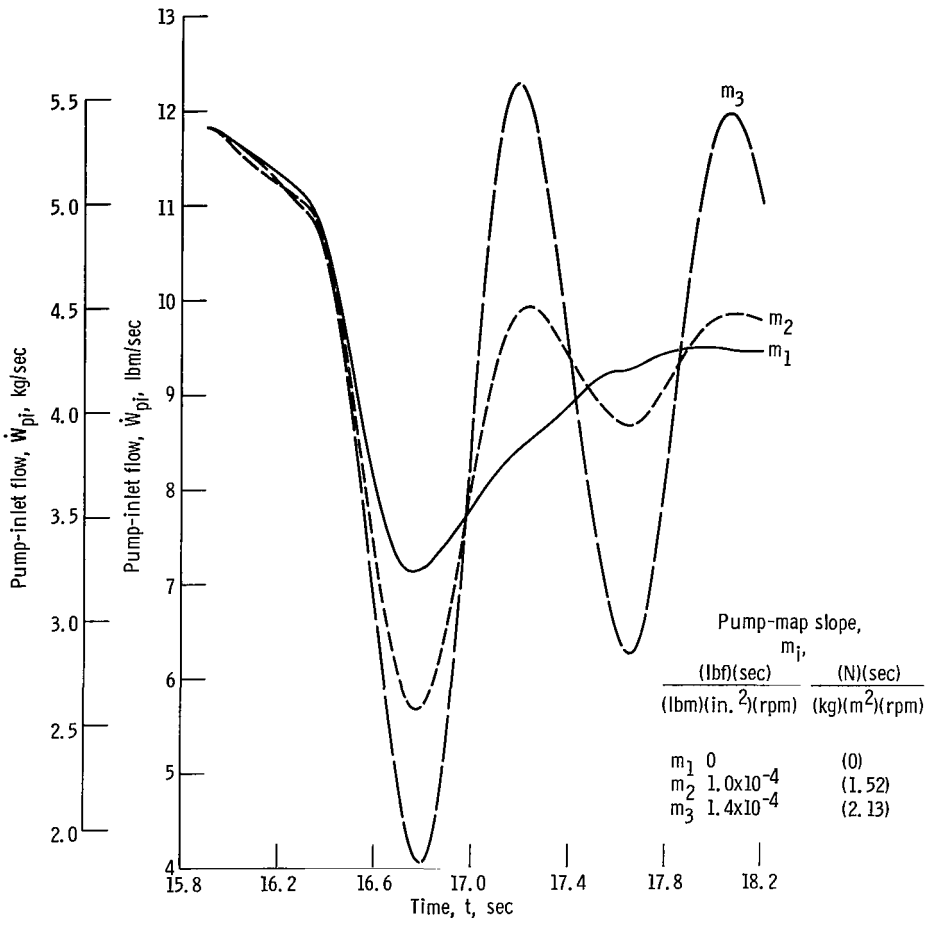

(a) For in-stall variations; time period beginning at t = 15.9 seconds.

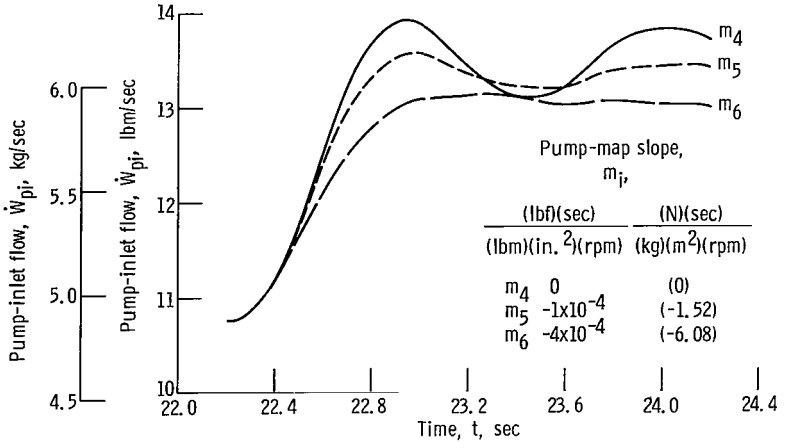

(b) For out-of-stall variations; time period beginning at t = 22.2 seconds.

Figure 20. - Axial-pump-inlet flow resulting from pump-map-slope variations.

crease in solution damping supports the theory that overall system instability can result if the slope of inlet-pumping characteristics becomes too positive (ref. 4).

Radial-pump system. - The pump operates out-of-stall during the speed disturbance considered. The steady-state pump map was derived from a series of special pump tests, and a portion of the out-of-stall region is compared with the axial pump map in figure 21. As illustrated in the figure, a particular characteristic of the radial pump is the presence of positive slopes in the out-of-stall region. The solution (beginning at t = 13.5 sec) operates in the positively sloped region of the map.

The sensitivity of the system to the slope of the pump map is similar to that observed for the axial-pump system. To demonstrate this, a pump-inlet-flow solution using a zero

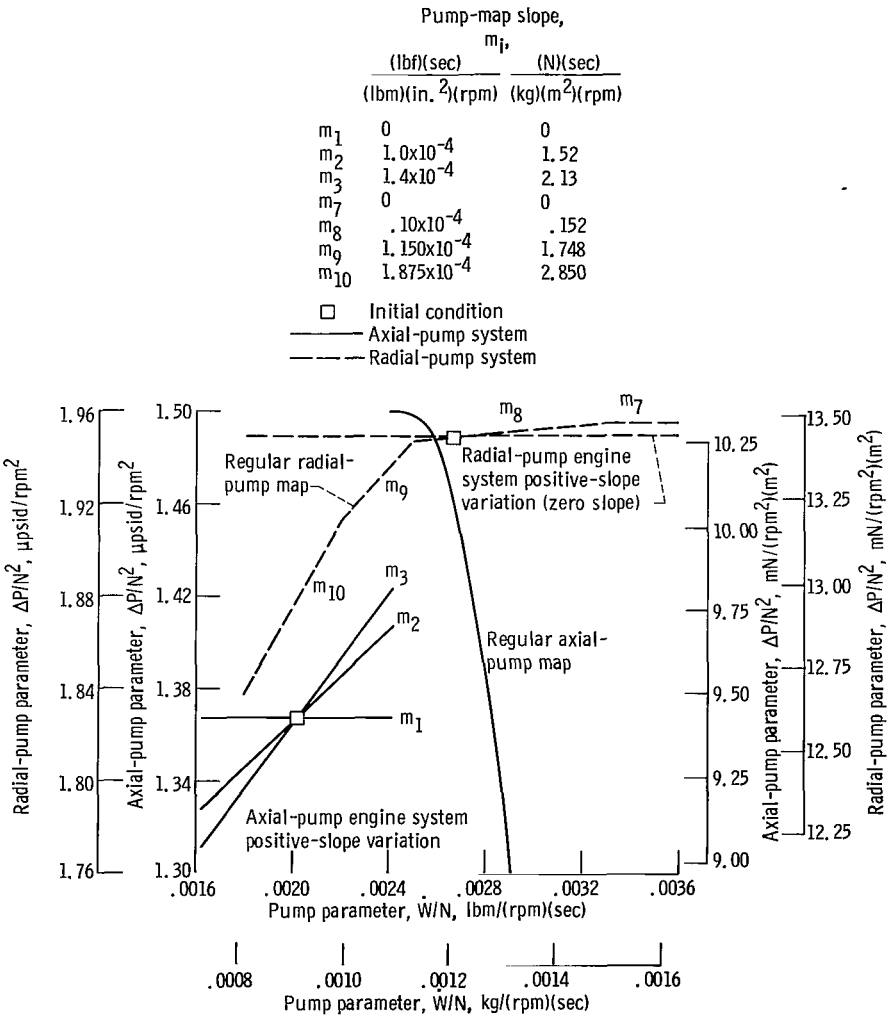

Figure 21. - Positive-slope pump-map variations for axial- and radial-pump systems.

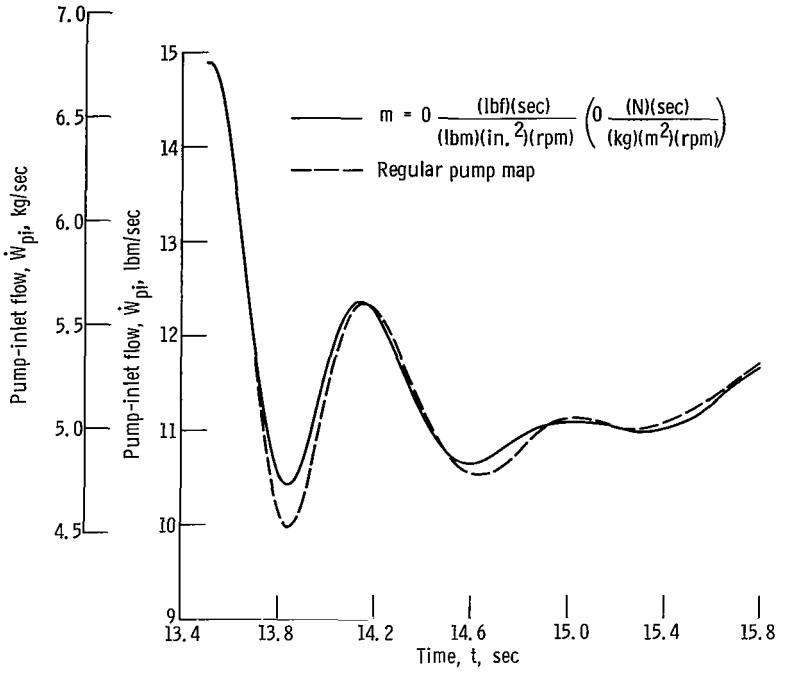

Figure 22. - Radial-pump system pump-inlet flow solutions using zero and regular pump-map slopes.

pump-map slope is compared in figure 22 with a solution using the regular pump map. The regular-pump-map solution is more oscillatory due to the positive slopes of the pump map.

The difference between the regular-pump-map solution and the zero-pump-map solution, however, is much smaller for this engine system than it was for the in-stall axial-pump system (fig. 20(a)). The difference is mainly attributed to the more oscillatory pump-speed forcing function which is used with the radial pump. As presented earlier while discussing figure 8, the radial-pump system response to the speed demand was less damped. The resulting pump-speed waveform, shown in figure 8(c), has a small oscillation superimposed on the general smooth trend.

Another factor which contributes to the more oscillatory radial-pump system response is the longer pump-inlet feedline. The effect of the longer line is to increase the amount of fluid (liquid) inertia. However, this reduced-damping effect is small because of the large diameter of the pump-inlet feedline and the relatively large amount of liquid inertia existing downstream of the pump.

Importance of Correct Averaging

When the modeling technique for a system uses gross spatial lumps as approximations to the spatial dependence of the describing partial differential equations, the type of lump averaging becomes important. In particular, when treating the mass-flow storage in the nuclear-rocket cold-flow engine systems described, a special type of averaging technique proved necessary.

It was found in the analysis in appendix A, that to approximate the mass-flow storage in a gross fluid-lump it is necessary to calculate the average value of the thermodynamic fluid property $[\partial\rho/\partial P]_h$. Simulation of the observed low-frequency flow dynamics, in fact, hinges also on the continued updating of this average. Hence, the average values for pressure, density, and enthalpy in the two-phase fluid-lump are related as follows:

$$P_{2p} = P(\rho_{2p,av},\ h_{2p,av})$$

and

$$h_{2p,av} = h\left(\left[\frac{\partial\rho}{\partial P}\right]_{h,av},\ P_{2p}\right)$$

(Throughout the equations in this report, parentheses are used solely for functional notation, and brackets and braces are used for all other purposes.) A set of curves for the second expression is derivable from the hydrogen-properties tables in reference 3.

To demonstrate the importance of calculating the correct average for $h_{2p,av}$, two basic averaging schemes are compared: (1) relating $h_{2p,av}$ to the arithmetic spatial average of $[\partial\rho/\partial P]_h$, and (2) calculating the arithmetic spatial average of $h_{2p,av}$. For each scheme, the effect of holding the average at its initial value during the solution is also considered. The solutions shall be referred to as those resulting from the following enthalpy-averaging techniques:

(1) The average two-phase fluid enthalpy $h_{2p,av}$ predicted by the previous equations, with the average thermodynamic fluid property updated continually in high-speed, repetitive operation by the equation

$$\left[\frac{\partial\rho}{\partial P}\right]_{h,av} = \frac{\int_{X_{sl}}^{X_{sg}} \left[\frac{\partial\rho}{\partial P}\right]_h (x)\,dx}{X_{sg} - X_{sl}}$$

(2) The $h_{2p,av}$ predicted as in (1) but with $[\partial\rho/\partial P]_{h,av}$ calculated once and then held constant throughtout the computer solution.

(3) The $h_{2p,av}$ predicted by the equation

$$h_{2p,av} = \frac{\int_{X_{sl}}^{X_{sg}} h_{2p}(x)\,dx}{X_{sg} - X_{sl}}$$

continually in high-speed, repetitive operation.

(4) The $h_{2p,av}$ predicted as in (3) but with the average held constant at its initial value throughout the computer solution.

The results for both engine systems are consistent. The solution for pump-inlet flow which is closest to experimental data uses enthalpy-averaging technique (1), that is, the technique which helps establish the correct mass-flow storage in the system. The curves in figure 23 show the results of using the four averaging techniques for the down-speed-step radial-pump system simulation. The results for the axial-pump system are similar.

Comparing figure 23(c) with 23(a) demonstrates the effect of using an arithmetic spatial averaging technique for $h_{2p,av}$. The curve in figure 23(c) is characteristic of a system with less capacitance, or storing capability. The period and the amplitude of oscillation are both reduced.

The importance of continually updating $h_{2p,av}$ is evident by comparing figure 23(a) with 23(b) and figure 23(c) with 23(d). The solution in figure 23(b) is continuous; the plotting was merely discontinued and then resumed at the x-axis. The $h_{2p,av}$ from technique (1) never changed more than 16 percent from its initial value during the total solution.

The predicted mass-flow storage in the system is obtained by taking the difference between the predicted values of pump-inlet flow and thrust-nozzle-chamber flow. The curves in figure 24 show the predicted mass-flow storage which results from using each of the four enthalpy-averaging techniques. The calculated values shown are determined from experimental values of pump-inlet flow and calculated values of thrust-nozzle-chamber flow. These results are presented, for the positive-speed-step axial-pump system simulation, since they most clearly illustrate the effect of the enthalpy-averaging technique on the system mass-flow storage. The best solution (shown in fig. 24(a)) uses enthalpy-averaging technique (1). Whereas an obvious lack of mass-flow storage is illustrated in figure 24(c).

By comparing figure 24(a) with 24(b) and figure 24(c) with 24(d) the significance of continually updating the average two-phase fluid enthalpy becomes obvious. During the

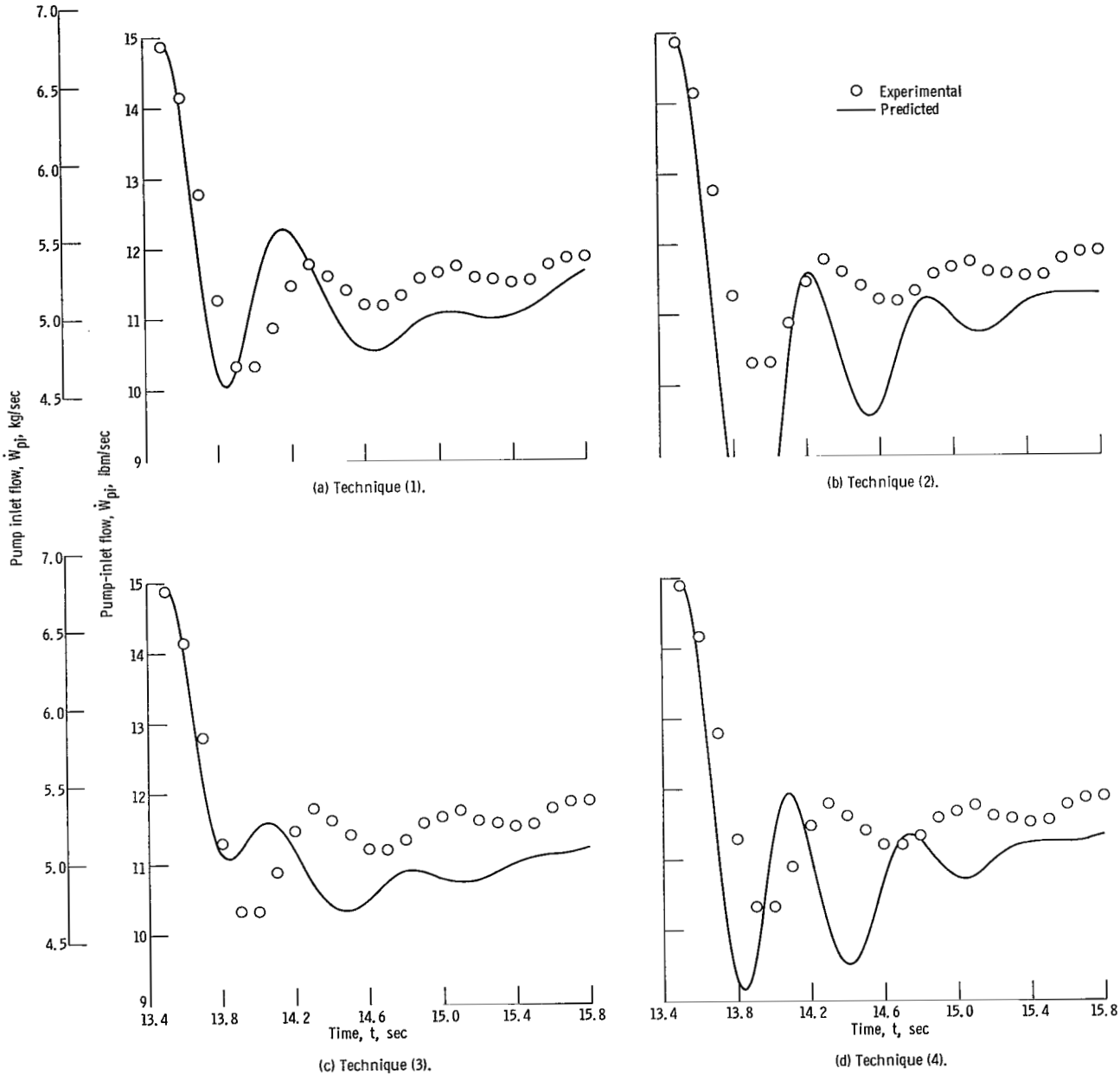

(a) Technique (1).

(b) Technique (2).

(c) Technique (3).

(d) Technique (4).

Figure 23. - Radial-pump system pump-inlet flow resulting from enthalpy-averaging techniques.

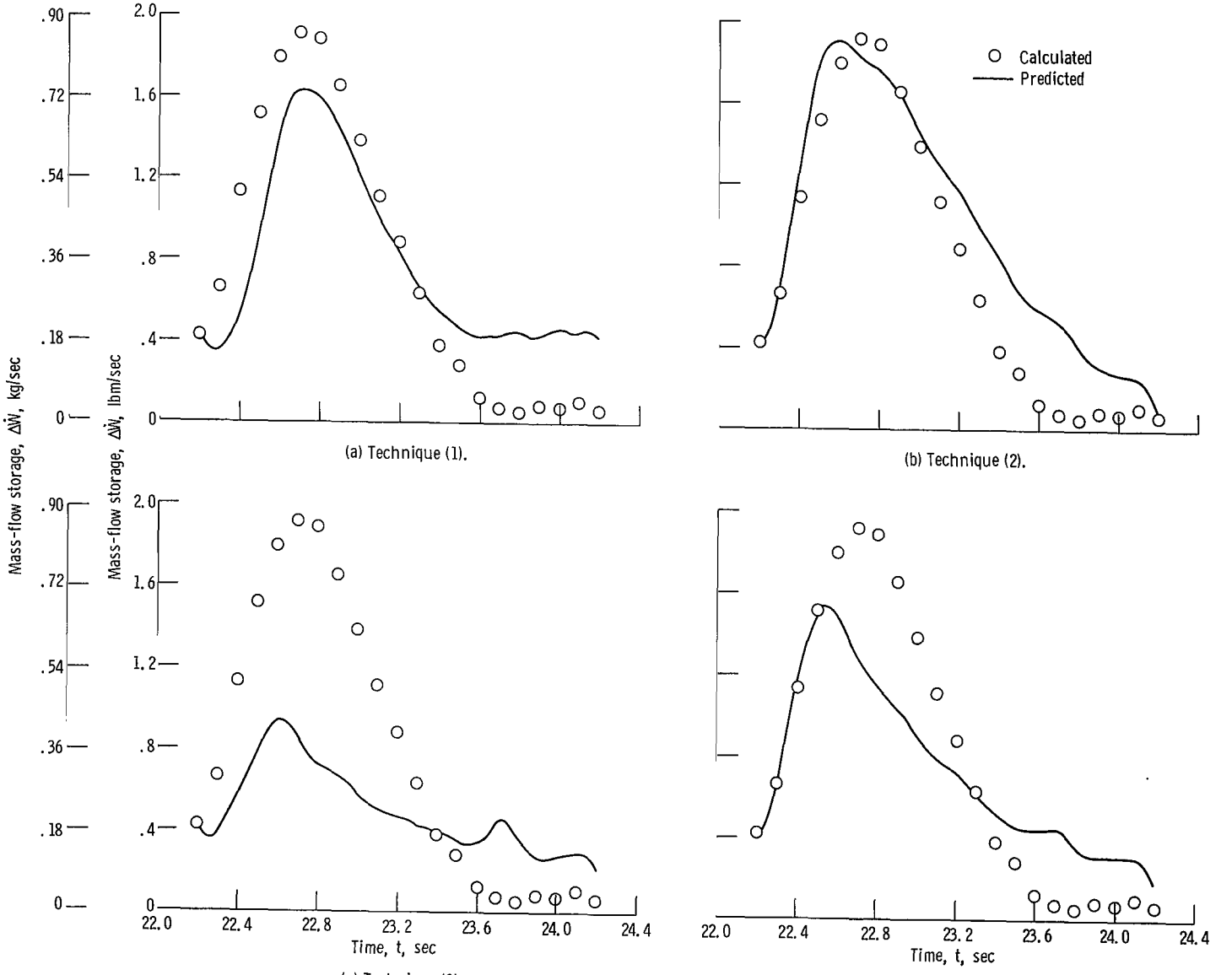

(a) Technique (1).

(b) Technique (2).

(c) Technique (3).

(d) Technique (4).

Figure 24. - Axial-pump system pump-inlet to core-exit flow storage resulting from using enthalpy-averaging technique.

solution, the $h_{2p,av}$ from technique (1) never changed more than 3 percent from its initial value.

Additional Effects

Nozzle-inlet-manifold fluid enthalpy. - An important forcing function is the nozzle-inlet-manifold fluid enthalpy h_{ni}. The magnitude of h_{ni} has a large effect on the computer solution since its value defines a reference point for the fluid-enthalpy x-distribution calculations. Consider the errors $\Delta T_{b,e}$ and ΔP_e in the measured values of nozzle-inlet-manifold fluid temperature and pressure, respectively. The resulting error in the fluid enthalpy would be

$$\Delta h_e = \left[\frac{\partial h}{\partial T}\right]_P \Delta T_{b,e} + \left[\frac{\partial h}{\partial P}\right]_T \Delta P_e$$

For liquid-hydrogen fluid, the more dominant error term is that due to the fluid temperature error, such that

$$\Delta h_e \approx \left[\frac{\partial h}{\partial T}\right]_P \Delta T_{b,e}$$

The curves in figure 25 show the appreciable effect on the pump-inlet-flow solution of 0.5 and -0.5 Rankine degrees (±0.278 K) errors in the measured value of the nozzle-inlet-manifold fluid temperature. The higher temperature fluid results with a value of h_{ni} closer to the value of saturated-liquid enthalpy. Hence, a higher value of $T_{b,ni}$ necessarily corresponds to a larger two-phase volume because of the relatively low input heat flux of the nozzle-coolant tubes.

It is shown in reference 4 that the presence of a boiling, two-phase compressible volume can reduce the system stability and make it more oscillatory. The curves in figure 25 support this, since the most oscillatory solution is obtained with the warmest fluid. The relatively large effect of the temperature change, however, was not expected.

Use of steady-state pump map. - The pump operating point is assumed defined at all times on a steady-state pump map. In general, this may not be the case, since the solutions contain large transients. Significant deviations from the steady-state characteristics can take place under certain transient conditions. Based on the response sensitivity observed in the pump-map-slope parametric variations, the introduction of pump dynamics into the model could have a meaningful effect of the solutions.

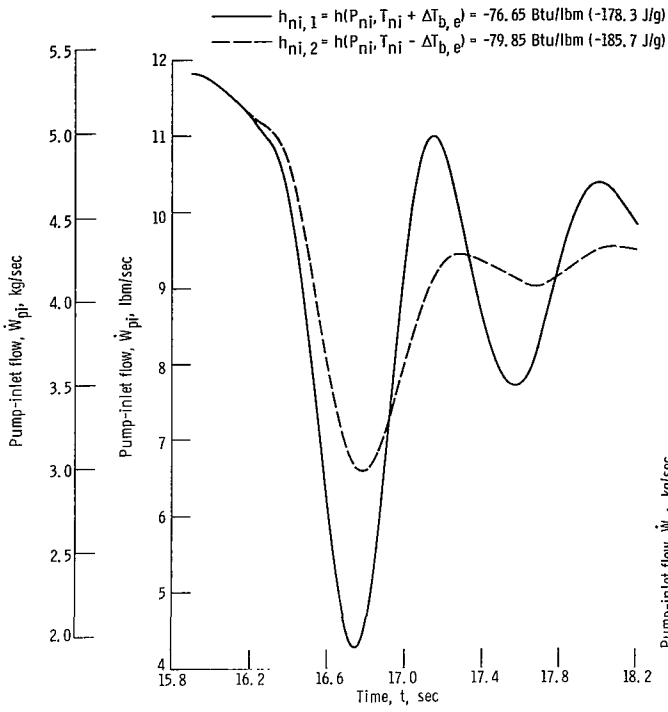

(a) For the axial-pump system time period beginning at t = 15.9 seconds.

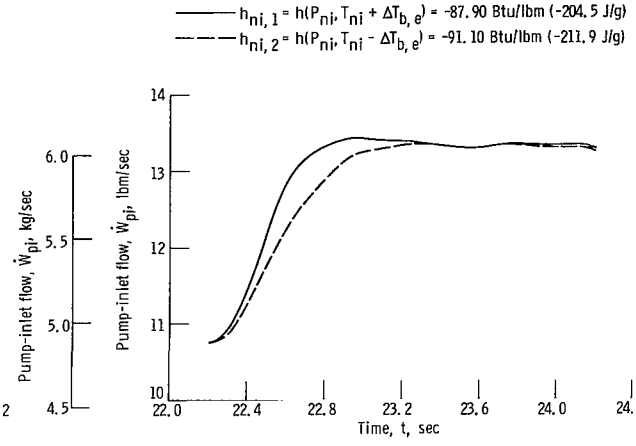

(b) For the axial-pump system time period beginning at t = 22.2 seconds.

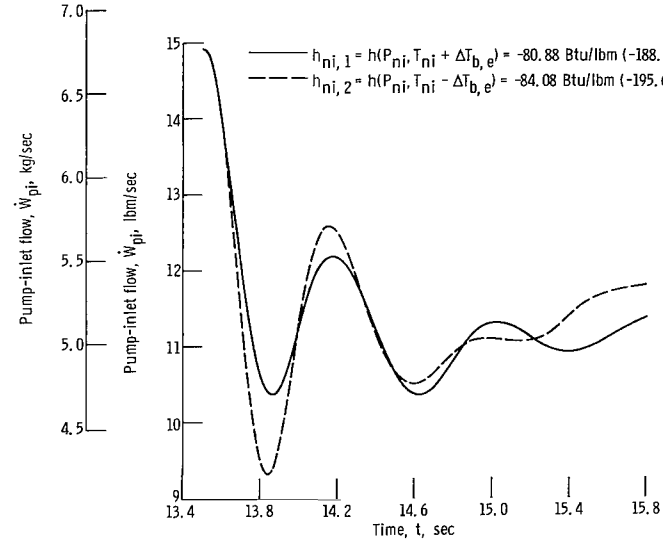

(c) For the radial-pump system time period.

Figure 25. - Pump-inlet flow resulting from two different initial conditions on nozzle-inlet-manifold fluid enthalpy.

SUMMARY OF RESULTS

Simplified models of two nuclear-rocket cold-flow engine systems were programmed on an analog computer to study the mechanisms governing the observed low-frequency flow dynamics. A summary of the results of this study are as follows:

1. An adequate two-phase state equation for the case when thermodynamic equilibrium may be assumed between the gas and liquid phases is

$$P_{2p} = \rho_{2p}[\alpha(P_{2p}) + \beta(P_{2p})h_{2p}]$$

where P_{2p} is the two-phase fluid pressure, ρ_{2p} is the two-phase fluid density, h_{2p} is the two-phase fluid enthalpy, and α and β are coefficients which are functions of pressure.

2. The key to obtaining a low-frequency response is to obtain the proper mass-flow storage. This is achieved by relating the average fluid enthalpy of a fluid-lump to the average value of the thermodynamic property $[\partial\rho/\partial P]_h$; that is,

$$h_{av} = h\left(P_{av}, \left[\frac{\partial\rho}{\partial P}\right]_{h,\,av}\right)$$

$$P_{av} = P(\rho_{av}, h_{av})$$

where $[\partial\rho/\partial P]_h$ is the partial derivative of density with respect to pressure (enthalpy held constant), P is the fluid pressure, ρ is the fluid density, h is the fluid enthalpy, and the subscript av indicates an average quantity.

3. Analysis shows that most of the mass-flow storage occurs in the region of low mass quality, that is, in the two-phase fluid in the neighborhood of the saturated-liquid boundary.

4. The pump operating-characteristics can significantly affect the system damping. In fact, operation on positive pump-map slopes reduces the overall system damping.

The following remarks are made concerning the analytical model used: The magnitude of nozzle-inlet-manifold fluid enthalpy is important since it defines a reference point for the fluid-enthalpy x-distribution calculations. Introducing the possible experimental error in determining this forcing function results in significant changes in the solution for pump-inlet flow.

A small amount of computational instability occurred with the combined operation of the slow-speed analog and the high-speed analog. The output from the high-speed track-and-store circuits was noisy and had to be filtered. It was found that the inherent errors

associated with the track-and-store units (±0.5 percent) would cause a sampled variable to become noisy. Whenever such an unfiltered variable was used in a relatively high-gain (×100) circuit, the entire simulation was unstable. The size of the required noise-filter capacitors, of course, depends on the repetitive operation rate.

Lewis Research Center,
National Aeronautics and Space Administration,
Cleveland, Ohio, February 11, 1969,
126-15-02-36-22.

APPENDIX A

DERIVATION OF VARIABLE-VOLUME EQUATIONS

Consider a gross, one-dimensional system lump, bounded by inlet and exit surfaces (which may be variable) and composed of l equal sublumps at any instant of time (see fig. 26). It is desired to approximate the proper mass-flow storage, pressure drop,

Figure 26. - Sublumping of gross, one-dimensional system lump.

and heat transfer for this section of the system by single equations of the respective forms

$$\Delta\dot{W}_{tot} = \frac{\partial}{\partial t}[\rho_{av}V_{tot}]$$

$$\Delta P_{tot} = \Delta P_{iner} + \Delta P_{fr} + \Delta P_{mom} + \Delta P_{gr}$$

$$\dot{Q}_{tot} = \sum_{i=1}^{l} \dot{Q}_i$$

Approximating Mass-Flow Storage

Mass-flow distribution for gross lump. - Consider first the system shown in figure 26 and assume that the bounding surfaces are fixed. The amount of mass-flow storage in the i^{th} sublump is given by

$$\Delta\dot{W}_i = \frac{\partial}{\partial t}[\rho_i V_i]$$

Hence, the total mass-flow storage would be

$$\Delta\dot{W}_{tot} = \frac{V_{tot}}{l}\sum_{i=1}^{l}\frac{\partial\rho_i}{\partial t}$$

The state equation of the fluid in the i^{th} sublump may be written as

$$\rho_i = \rho_i(P_i, h_i)$$

By the chain rule,

$$\frac{\partial\rho_i}{\partial t} = \left[\frac{\partial\rho}{\partial P}\right]_{h,\,i}\frac{\partial P_i}{\partial t} + \left[\frac{\partial\rho}{\partial h}\right]_{P,\,i}\frac{\partial h_i}{\partial t}$$

The total mass-flow storage, therefore, is

$$\Delta\dot{W}_{tot} = \frac{V_{tot}}{l}\sum_{i=1}^{l}\left[\frac{\partial\rho}{\partial P}\right]_{h,\,i}\frac{\partial P_i}{\partial t} + \frac{V_{tot}}{l}\sum_{i=1}^{l}\left[\frac{\partial\rho}{\partial h}\right]_{P,\,i}\frac{\partial h_i}{\partial t}$$

Figure 27 shows the two thermodynamic properties $[\partial\rho/\partial P]_h$ and $-[\partial\rho/\partial h]_P$ for 100 percent parahydrogen as a function of fluid enthalpy. The curves were calculated for constant pressures of 5, 20, and 80 psia (34, 138, and 552 kN/m^2) from the data on hydrogen properties in reference 3. The variations of the two thermodynamic properties are shown for the liquid, two-phase, and gaseous fluid states. The vertical dotted lines are located at the values of saturated-liquid and saturated-gas enthalpies.

The pressure and enthalpy rate of change terms (the time derivatives) are assumed approximately uniform throughout a variable-volume lump. Therefore, we can write

$$\Delta\dot{W}_{tot} = V_{tot}\left[\frac{\partial P}{\partial t}\right]_{av}\frac{1}{l}\sum_{i=1}^{l}\left[\frac{\partial\rho}{\partial P}\right]_{h,\,i} + V_{tot}\left[\frac{\partial h}{\partial t}\right]_{av}\frac{1}{l}\sum_{i=1}^{l}\left[\frac{\partial\rho}{\partial h}\right]_{P,\,i}$$

$$= V_{tot}\left[\frac{\partial P}{\partial t}\right]_{av}\left[\frac{\partial\rho}{\partial P}\right]_{h,\,av} + V_{tot}\left[\frac{\partial h}{\partial t}\right]_{av}\left[\frac{\partial\rho}{\partial h}\right]_{P,\,av}$$

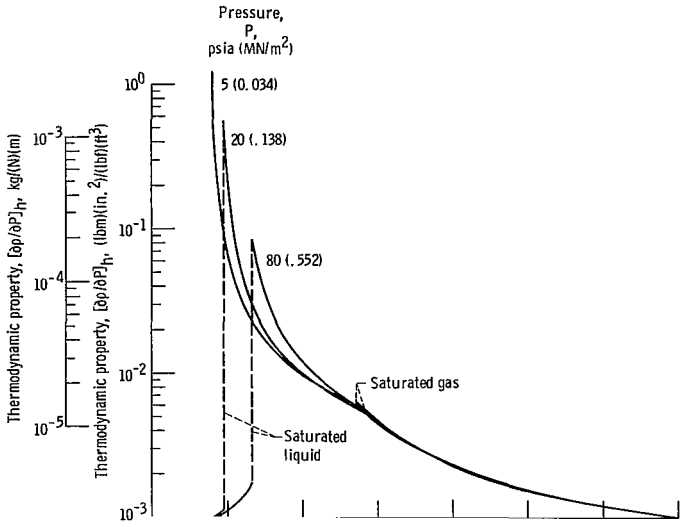

(a) Partial derivative of density with respect to pressure (enthalpy held constant).

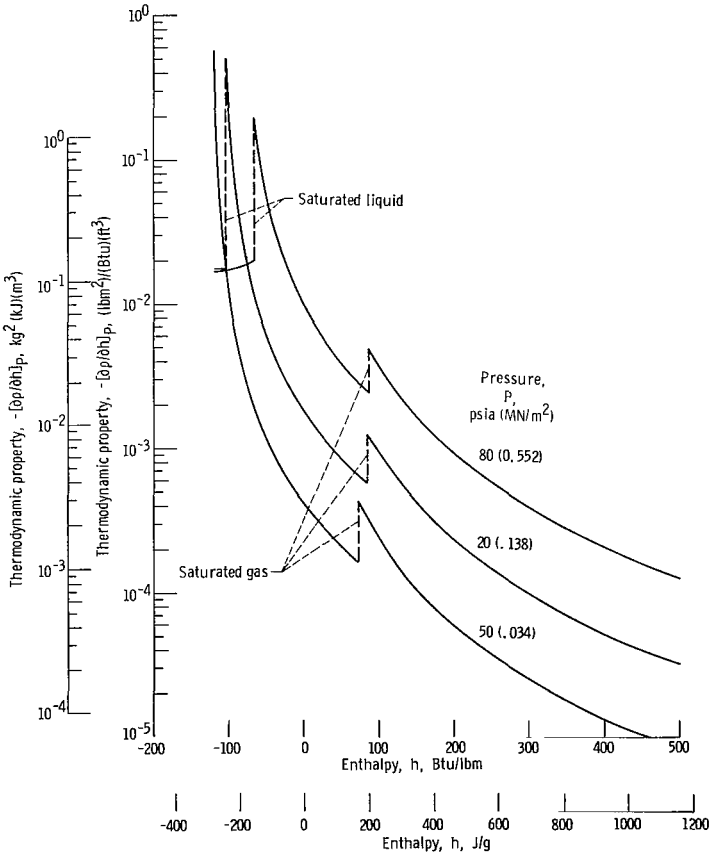

(b) Partial derivative of density with respect to enthalpy (pressure held constant).

Figure 27. - Three constant-pressure lines of thermodynamic properties as function of enthalpy.

The maximum mass-flow storage occurs at the point in the lump where $[\partial\rho/\partial P]_h$ and $[\partial\rho/\partial h]_h$ are largest. Clearly, the most mass-flow accumulation will take place in the two-phase fluid. In addition, it is evident that most of this mass-flow storage will occur in regions of low mass quality, that is, in the vicinity of the saturated-liquid boundary.

Experimental data indicate that for the system under study the enthalpy time rate of change term is small compared with the pressure time rate of change term. An approximate expression for the total mass-flow storage, therefore, is

$$\Delta\dot{W}_{tot} = V_{tot}\left[\frac{\partial\rho}{\partial P}\right]_{h,\,av}\left[\frac{\partial P}{\partial t}\right]_{av}$$

Hence, average values for pressure, density, and enthalpy will be related through the average value of the thermodynamic property $[\partial\rho/\partial P]_h$. Mathematically, this may be written as

$$h_{av} = h\left(P_{av}, \left[\frac{\partial\rho}{\partial P}\right]_{h,\,av}\right)$$

and

$$P_{av} = P(\rho_{av},\ h_{av})$$

Continuity equation for gross lump. - For the constant-volume approach the mass-flow storage may be written as

$$\Delta\dot{W}_{tot} = \dot{W}_{in} - \dot{W}_{out}$$

For the variable-volume approach, however, the inlet and exit boundaries are variable. If the inlet boundary moves with a velocity $U_{B,\,in}$ and the exit boundary moves with a velocity $U_{B,\,out}$, the mass-flow storage equation becomes

$$\Delta\dot{W}_{tot} = [\dot{W} - \rho A U_B]_{in} - [\dot{W} - \rho A U_B]_{out}$$

The continuity equation for the gross lump, therefore, may be written as

$$\frac{\partial}{\partial t}[\rho_{av} V_{tot}] = [\dot{W} - \rho A U_B]_{in} - [\dot{W} - \rho A U_B]_{out}$$

Approximating Pressure Drop

Consider similar sublumping as in the previous section. The pressure drop across the i^{th} sublump would be

$$\Delta P_{tot,\,i} = \Delta P_{iner,\,i} + \Delta P_{fr,\,i} + \Delta P_{mom,\,i} + \Delta P_{gr,\,i}$$

The total pressure drop across the gross lump would be

$$\Delta P_{tot} = \sum_{i=1}^{l} \Delta P_{tot,\,i}$$

$$= \sum_{i=1}^{l} \Delta P_{iner,\,i} + \sum_{i=1}^{l} \Delta P_{fr,\,i} + \sum_{i=1}^{l} \Delta P_{mom,\,i} + \sum_{i=1}^{l} \Delta P_{gr,\,i}$$

The individual terms will now be considered. Assume that each sublump has constant flow area (the sublumps need not be of equal length). Consider only the geometry variations between sublumps. Assume that flow is uniform.

Total inertia pressure drop. -

$$\Delta P_{iner} = \sum_{i=1}^{l} \Delta P_{iner,\,i} = \frac{1}{ng} \sum_{i=1}^{l} \frac{1}{A_i} \frac{\partial}{\partial t} \left[\mathring{W}\, \Delta X\right]_i$$

$$\approx \frac{1}{ng} \left[\sum_{i=1}^{l} \frac{\Delta X_i}{A_i}\right] \frac{\partial \dot{W}_{av}}{\partial t}$$

Total friction pressure drop. - For circular passages

$$\Delta P_{fr} = \sum_{i=1}^{l} \Delta P_{fr,\,i} = \frac{\pi}{n} \sum_{i=1}^{l} \left[\frac{\tau_w D\, \Delta X}{A}\right]_i$$

The coefficient of friction (ref. 5) is usually defined as

$$f \equiv \frac{2g\tau_w}{\rho_b U_b^2}$$

For turbulent flow with $Re \leq 200\,000$ an approximate expression is

$$f = \frac{0.046}{Re^{0.2}}$$

$$= 0.046 \left[\frac{\mu_f A}{\dot{W} D}\right]^{0.2}$$

where the viscosity is to be evaluated at the film temperature and pressure. Bends and entrance effects may be included in an additional loss term K_{loss}. The effective wall shear of the i^{th} sublump may, therefore, be written as

$$\tau_{w,i} = \frac{0.023}{g A_i \Delta X_i} \left[\frac{D}{A}\right]_i^{0.8} \left[\frac{L}{D}\right]_{eff,i} \left[\frac{\mu_f}{\dot{W}}\right]_i^{0.2} \left[\frac{\dot{W}^2}{\rho_b}\right]_i$$

for liquid and gas, and

$$\tau_{w,i} = \frac{0.023}{g A_i \Delta X_i} \left[\frac{D}{A}\right]_i^{0.8} \left[\frac{L}{D}\right]_{eff,i} \left[\frac{\mu_f}{\dot{W}}\right]_i^{0.2} \left[\frac{\rho_f}{\rho_b}\right]^{0.8} \left[\frac{\dot{W}^2}{\rho_b}\right]_i$$

for two-phase fluid (appendix C), where

$$\left[\frac{L}{D}\right]_{eff,i} = \frac{\Delta X_i}{D_i} + K_{loss,i}$$

Hence, the following equation approximately represents the total friction pressure drop:

$$\Delta P_{fr} = \frac{0.023\,\pi}{ng}\left\{\sum_{i=1}^{l}\frac{D_i^{1.8}}{A_i^{2.8}}\left[\frac{L}{D}\right]_{eff,\,i}\right\}\left[\frac{\mu_f}{\dot{W}}\right]_{av}^{0.2}\frac{\dot{W}_{av}^2}{\rho_{av}}$$

for liquid and gas, and

$$\Delta P_{fr} = \frac{0.023\,\pi}{ng}\left\{\sum_{i=1}^{l}\frac{D_i^{1.8}}{A_i^{2.8}}\left[\frac{L}{D}\right]_{eff,\,i}\right\}\left[\frac{\mu_f}{\dot{W}}\right]_{av}^{0.2}\left[\frac{\rho_f}{\rho}\right]_{av}^{0.8}\frac{\dot{W}_{av}^2}{\rho_{av}}$$

for two-phase fluid (appendix C), where

$$\rho_{av} = \frac{2\rho_{in}\rho_{out}}{\rho_{in} + \rho_{out}}$$

An average value of film viscosity is assumed.

Total memontum pressure drop. -

$$\Delta P_{mom} = \sum_{i=1}^{l}\Delta P_{mom,\,i} = \frac{1}{ng}\sum_{i=1}^{l}\frac{\dot{W}_i}{A_i}\left\{\frac{\left[\dot{W} - \rho A U_B\right]_{out}}{\rho_{out}A_{out}} - \frac{\left[\dot{W} - \rho A U_B\right]_{in}}{\rho_{in}A_{in}}\right\}_i$$

A more convenient and approximate form for this equation is

$$\Delta P_{mom} \approx \frac{1}{ngV_{tot}}\left\{\sum_{i=1}^{l}\left[\frac{\Delta X}{A}\right]_i\right\}\left[\frac{\dot{W}_{out}^2}{\rho_{out}} - \frac{\dot{W}_{in}^2}{\rho_{in}}\right]$$

It is assumed that the area change from sublump to sublump is accounted for with the loss term in the friction pressure-drop equation. The preceeding expression for the complete

momentum pressure drop, although only an approximate representation, provides a convenient variable coefficient for analog computer solution.

Total gravity pressure drop. -

$$\Delta P_{gr} = \sum_{i=1}^{l} \Delta P_{gr,i} = \frac{Z_{out} - Z_{in}}{n} \frac{1}{l} \sum_{i=1}^{l} \rho_i$$

$$= \frac{\rho'_{av} \Delta Z_{tot}}{n}$$

Momentum equation for gross lump. - Beginning with the complete pressure drop equation

$$\Delta P_{tot} = \Delta P_{iner} + \Delta P_{fr} + \Delta P_{mom} + \Delta P_{gr}$$

the following form of the momentum equation for the gross lump may be derived:

$$\frac{\partial \dot{W}}{\partial t} = a\left[\Delta P_{tot} - \frac{\rho'_{av} \Delta Z_{tot}}{n}\right] + bv_{av}\dot{W}^2_{av} + c\left[\frac{\dot{W}^2_{out}}{\rho_{out}} - \frac{\dot{W}^2_{in}}{\rho_{in}}\right]$$

where

$$a = \frac{ng}{\sum_{i=1}^{l} \frac{\Delta X_i}{A_i}}$$

$$b = \frac{0.023\,\pi \left\{ \sum_{i=1}^{l} \frac{D_i^{1.8}}{A_i^{2.8}} \left[\frac{L}{D}\right]_{eff,i} \right\} \left[\frac{\mu_f}{\dot{W}}\right]^{0.2}_{av}}{\sum_{i=1}^{l} \frac{\Delta X_i}{A_i}}$$

for liquid and gas, and

$$b = \frac{0.023\,\pi \left\{ \sum_{i=1}^{l} \frac{D_i^{1.8}}{A_i^{2.8}} \left[\frac{L}{D}\right]_{eff,i} \right\} \left[\frac{\mu_f}{\dot{W}}\right]_{av}^{0.2} \left[\frac{\rho_f}{\rho}\right]_{av}^{0.8}}{\sum_{i=1}^{l} \frac{\Delta X_i}{A_i}}$$

for two-phase fluid,

$$c = \frac{1}{V_{tot}} = \frac{1}{\sum_{i=1}^{l} A_i \Delta X_i}$$

and

$$v_{av} \equiv \left[\frac{1}{\rho}\right]_{av} = \frac{\rho_{in} + \rho_{out}}{2\rho_{in}\rho_{out}}$$

Approximating Heat Transfer

Consider the same sublumping as in the previous two sections. The heat flux in the i^{th} sublump from the wall to the fluid is

$$\dot{Q}_i = \mathcal{H}_i A_{ht,i} [T_{w,i} - T_{b,i}]$$

The total heat flux for the gross lump is then

$$\dot{Q}_{tot} = \sum_{i=1}^{l} \dot{Q}_i \approx \left[\sum_{i=1}^{l} \mathcal{H}_i A_{ht,i}\right] [T_w - T_b]$$

where an average wall-to-fluid temperature difference is assumed.

In this study heat transfer as a gross lump will only be considered in the gas fluid-lump. The heat-transfer coefficient is determined from the conventional correlation in reference 5; that is,

$$Nu_b = 0.023\, Re_b^{0.8} Pr_b^{0.4}$$

where the fluid properties are evaluated at the bulk fluid temperature. The heat-transfer coefficient for the i^{th} sublump would be

$$\mathcal{H}_i = \frac{0.023}{D_i^{0.2} A_i^{0.8}} \frac{k_i}{\mu_i^{0.8}} \left[\frac{c_p \mu}{k}\right]_i^{0.4} \dot{W}_i^{0.8}$$

Hence the gross-lump heat flux becomes

$$\dot{Q}_{tot} = C_{ht} F \dot{W}^{0.8} [T_w - T_b]$$

where the effective-geometry coefficient is

$$C_{ht} = 0.023 \sum_{i=1}^{l} \frac{A_{ht,i}}{D_i^{0.2} A_i^{0.8}}$$

and the fluid-properties coefficient is

$$F = \left[\frac{k^{0.6} c_p^{0.4}}{\mu^{0.4}}\right]_{T_b = T_{b,av}}$$

Effective-Geometry Coefficients

The effective-geometry coefficients are a, b, and c for the momentum equation and C_{ht} for the energy equation. Each coefficient contains at least one summation,

which is performed over the length of fluid-lump. Consider, for instance, the volume summation

$$V = \sum_{i=1}^{l} A_i \, \Delta X_i$$

The l sublumps are chosen so that they correspond to lengths of component hardware with a constant cross-sectional area. The pump-discharge feedline, downstream from the main flow-control valve, is an example of a sublump. The cross-sectional area is uniform for an approximately 18-foot (5.49-m) length.

A curve of the total, accumulative volume for the axial-pump engine system from the pump exit to the core exit may be made (see fig. 28). The pump discharge is selected as the origin (the three-fluid-lump model begins at the pump discharge). The first linear segment of the curve represents the constant-area feedline from the pump exit to the

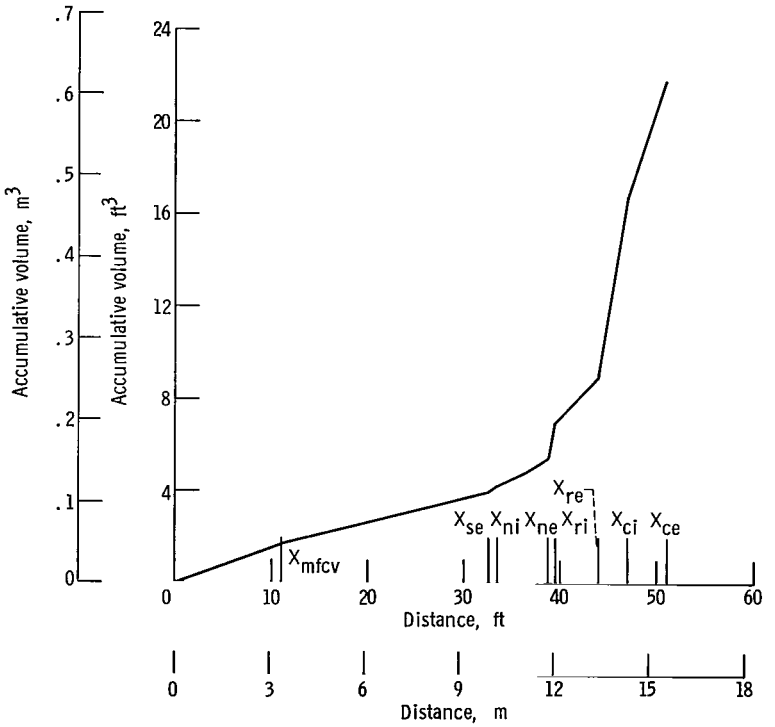

Figure 28. - Accumulative volume of axial-pump system from pump exit to core exit.

main flow-control valve. The remaining linear segments correspond to the other system components.

The total volume in the liquid fluid-lump may be computed from

$$V_{tot,\ell}(X_{s\ell}) = \sum_{i=1}^{\ell} V_i = \sum_{x=0}^{X_{s\ell}} V_x$$

This represents the point on the volume curve in the figure at $x = X_{s\ell}$. Clearly, the volumes of all three fluid-lumps are readily calculated from three points ($X_{s\ell}$, X_{sg}, and X_{ce}) on the accumulative volume curve; that is,

$$V_{tot,\ell}(X_{s\ell}) = \sum_{x=0}^{X_{s\ell}} V_x$$

$$V_{tot,2p}(X_{s\ell}, X_{sg}) = \sum_{x=0}^{X_{sg}} V_x - V_{tot,\ell}(X_{s\ell})$$

$$V_{tot,g}(X_{sg}) = V_{tot,\ell,2p,g}(X_{ce}) - \sum_{x=0}^{X_{sg}} V_x$$

A similar argument may be made for each summation appearing in the effective-geometry coefficients. For each summation, accumulative curves may be derived, which represent the system from the pump discharge to the core exit. The value of each summation, therefore, is available at any point $x\ (0 \le x \le X_{ce})$.

The effective-geometry coefficients are continuous functions of the positions of the two-phase fluid boundaries, $X_{s\ell}$ and X_{sg}. In addition, the friction pressure-drop coefficient b is also a function of flow $\dot{W}$. The coefficients may be written with the following functional notation.

Liquid fluid-lump:

$$a_l = a(X_{sl})$$

$$b_l = b(X_{sl}, \dot{W}_l)$$

$$c_l = c(X_{sl})$$

Two-phase fluid-lump:

$$a_{2p} = a(X_{sl}, X_{sg})$$

$$b_{2p} = b\left(X_{sl}, X_{sg}, \dot{W}_{2p}, \frac{\rho_{f,2p}}{\rho_{av,2p}}\right)$$

$$c_{2p} = c(X_{sl}, X_{sg})$$

Gas fluid-lump:

$$a_g = a(X_{sg})$$

$$b_g = b(X_{sg}, \dot{W}_g)$$

$$c_g = c(X_{sg})$$

APPENDIX B

TWO-PHASE EQUATION OF STATE

The two-phase fluid is assumed to be a uniform, homogeneous mixture of liquid and gas phases. For such a mixture, an average specific enthalpy and an average specific volume are defined as

$$h_{2p} = X_q h_{sg} + [1 - X_q] h_{s\ell} \tag{B1}$$

$$v_{2p} = X_q v_{sg} + [1 - X_q] v_{s\ell} \tag{B2}$$

where X_q is the mass quality, $h_{s\ell} = h_{s\ell}(P_{2p})$ is the saturated-liquid specific enthalpy, $h_{sg} = h_{sg}(P_{2p})$ is the saturated-gas specific enthalpy, $v_{s\ell} = v_{s\ell}(P_{2p})$ is the saturated-liquid specific volume, and $v_{sg} = v_{sg}(P_{2p})$ is the saturated-gas specific volume.

Eliminating mass quality X_q from equations (B1) and (B2) results in

$$v_{2p} = v_{s\ell} - \left[\frac{v_{sg} - v_{s\ell}}{h_{sg} - h_{s\ell}}\right] h_{s\ell} + \left[\frac{v_{sg} - v_{s\ell}}{h_{sg} - h_{s\ell}}\right] h_{2p} \tag{B3}$$

Multiplying both sides of equation (B3) by P_{2p} yields

$$P_{2p} v_{2p} = \alpha(P_{2p}) + \beta(P_{2p}) h_{2p} \tag{B4}$$

where

$$\alpha = P_{2p}\left\{v_{s\ell} - \left[\frac{v_{sg} - v_{s\ell}}{h_{sg} - h_{s\ell}}\right] h_{s\ell}\right\}$$

and

$$\beta = P_{2p}\left[\frac{v_{sg} - v_{s\ell}}{h_{sg} - h_{s\ell}}\right]$$

The variables α and β are well defined functions of the two-phase pressure P_{2p} and are shown in figure 29.

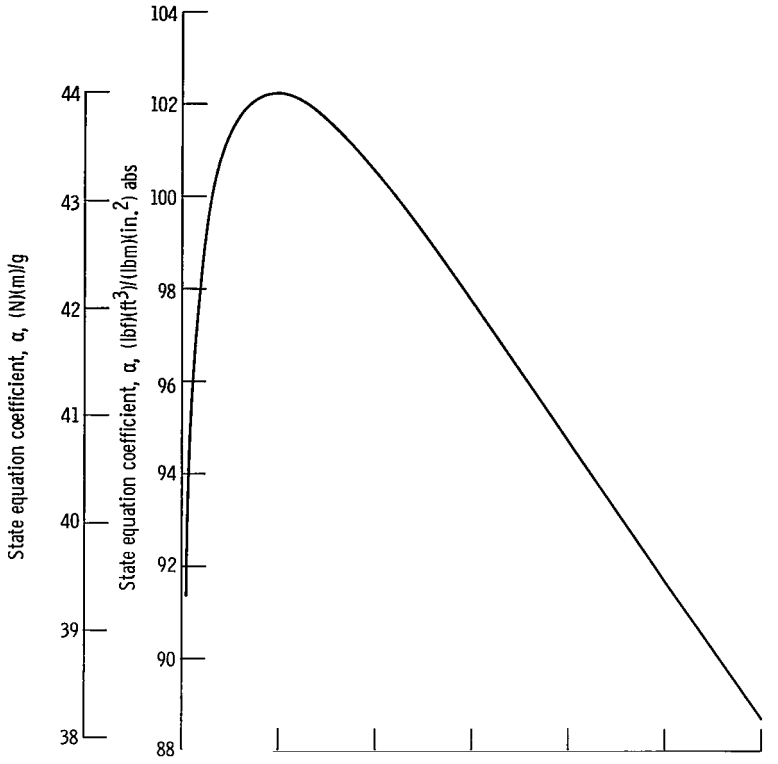

(a) Two-phase state equation coefficient α.

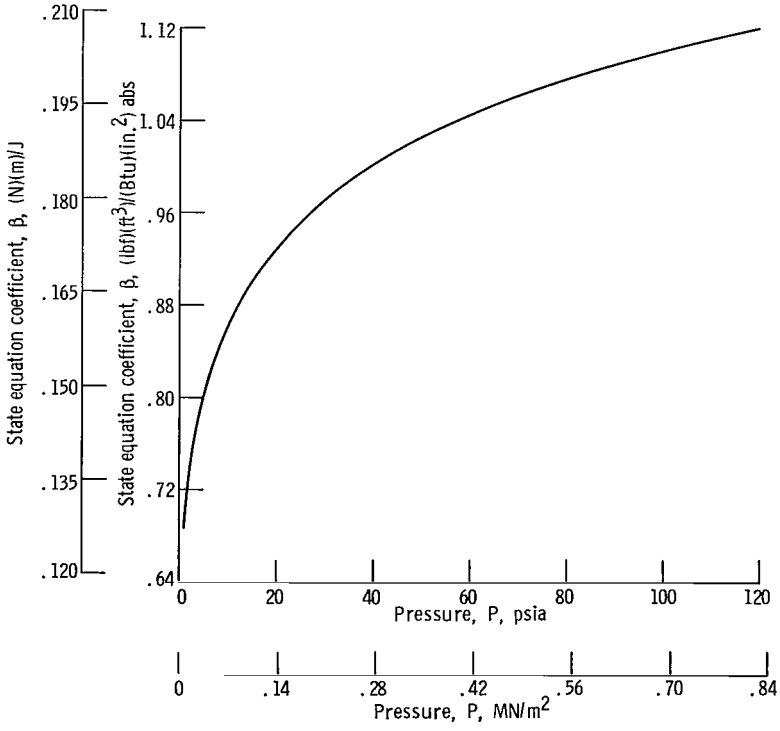

(b) Two-phase state equation coefficient β.

Figure 29. - State equation coefficients as functions of pressure.

Equation (B4) represents the two-phase equation of state. Since

$$\rho_{2p} \equiv \frac{1}{v_{2p}}$$

equation (B4) may be rewritten in terms of the two-phase density, such that

$$P_{2p} = \rho_{2p}[\alpha(P_{2p}) + \beta(P_{2p})h_{2p}] \tag{B5}$$

Given values for ρ_{2p} and h_{2p}, an algebraic balance of equation (B5) results in the proper value of P_{2p}.

APPENDIX C

FRICTION FACTOR FOR TWO-PHASE PRESSURE-DROP EQUATION

As discussed in the INTRODUCTION, the two-phase fluid was situated in the same general region of each engine system during the time periods of interest, namely, between the nozzle-inlet manifold and the reflector exit. Because of the high metal temperatures of the reflector and the nozzle-coolant-tubes shell, the two-phase fluid-lump is treated as a high wall-to-bulk temperature ratio region.

It is shown in reference 6 that the effect of high wall-to-bulk temperature ratios on the friction factor may be represented by the following correlation:

$$f = \left[\frac{\rho_f}{\rho_{av}}\right] f_f$$

where f_f is determined by a modified Reynolds number in which the density and viscosity are evaluated at the film temperature (midway between the fluid and wall temperatures). Hence, for turbulent flow with $Re \leq 200\ 000$, an approximate expression for the two-phase friction factor is

$$f_{2P} = \left[\frac{\rho_f}{\rho_{av}}\right]_{2p} \left[\frac{0.046}{Re_f^{0.2}}\right]_{2p}$$

$$= 0.046 \left[\frac{\rho_f}{\rho_{av}}\right]_{2p} \left[\frac{\mu_f}{\rho_{av} U_{av} D} \frac{\rho_{av}}{\rho_f}\right]_{2p}^{0.2}$$

$$= 0.046 \left[\frac{\rho_f}{\rho_{av}}\right]_{2p}^{0.8} \left[\frac{\mu_f A}{\dot{W} D}\right]_{2p}^{0.2}$$

APPENDIX D

MATHEMATICAL REPRESENTATION OF ENGINE SYSTEMS

Most of the variables are only functions of time. To simplify the equations, these variables are written without the function of time notation; that is, a typical variable y(t) is written simply y. However, some variables are either functions of both distance and time, or are functions only of distance. These variables are typically written as y(x,t) and y(x), respectively. For clarity, this notation is used only in the final step of lengthy equation derivations.

Tank

The run tank is treated as a constant-pressure, liquid-hydrogen supply. Hence,

$$P_t = \text{Constant}$$

Pump-Inlet Line

The all-liquid pump-inlet line is a stationary, constant-geometry lump. The equations derived in appendix A apply to this fluid-lump with stationary boundaries. Neglecting the momentum pressure drop yields

$$\frac{\partial \dot{W}_{pi}}{\partial t} = a_{pi}\left[P_t - P_{pi} - \frac{\rho_{pi}\,\Delta Z_{pi}}{n}\right] - b_{pi}\frac{\dot{W}_{pi}^2}{\rho_{pi}}$$

For small variations in fluid enthalpy,

$$\frac{\partial P_{pi}}{\partial t} = \frac{1}{V_{pi}}\left[\frac{\partial P}{\partial \rho}\right]_{h,pi}\left[\dot{W}_{pi} - \dot{W}_{\ell}\right]$$

the density ρ_{pi} and the geometry coefficients a_{pi}, b_{pi}, and V_{pi} are constants.

Pump

The pump operation is assumed to be defined by a normalized, steady-state map. The maps utilized were derived from experimental data and are shown in figure 7.

The set of defining equations for the pump is

$$\dot{W}_p = \frac{\dot{W}_{pi} + \dot{W}_l}{2}$$

$$N = N(t)$$

$$\frac{\Delta P_p}{N^2} = \frac{\Delta P_p}{N^2}\left(\frac{\dot{W}_p}{N}\right)$$

$$P_{po} = P_{pi} + N^2\left[\frac{\Delta P_p}{N^2}\right]$$

Pump Discharge to Core Exit

The three-fluid-lump model. - The liquid fluid-lump is characterized by a stationary upstream boundary at the pump discharge and by a variable downstream boundary at the saturated-liquid interface. The set of defining equations (appendix A) for the liquid fluid-lump is

$$\rho_l = \text{Constant}$$

$$\frac{\partial \dot{W}_l}{\partial t} = a_l[P_{po} - P_{2p}] - b_l\frac{\dot{W}_l^2}{\rho_l} - c_l\left[\frac{\dot{W}_{2p}^2}{\rho_{sl}} - \frac{\dot{W}_l^2}{\rho_l}\right]$$

$$a_l = a(X_{sl})$$

$$b_l = b(X_{sl}, \dot{W}_l)$$

$$c_l = c(X_{sl})$$

No mass-continuity equation is required since no mass-flow storage is assumed in this lump. An approximate value of nozzle-inlet-manifold pressure (for the high-speed analog) is

$$P_{ni} = P_{po} - \left[\frac{b_{ni}}{a_{ni}}\right]\frac{\dot{W}_l^2}{\rho_l}$$

where

$$\left[\frac{b_{ni}}{a_{ni}}\right] = \frac{b}{a}\,(X_{ni},\ \dot{W}_l)$$

The two-phase fluid-lump is bounded by two variable boundaries: the saturated-liquid boundary on the upstream side and the saturated-gas boundary on the downstream side. The boundary velocities $U_{B,\,sl}$ and $U_{B,\,sg}$ are approximated by analog derivative circuits. The defining equations are

$$\frac{\partial}{\partial t}\left[\rho_{2p,\,av} V_{2p}\right] = \dot{W}_l - \rho_{sl} A_{sl} U_{B,\,sl} - \dot{W}_{2p} + \rho_{sg} A_{sg} U_{B,\,sg}$$

$$V_{2p} = V(X_{sl}, X_{sg})$$

$$\rho_{sl} = \rho_{sl}(P_{2p})$$

$$\rho_{sg} = \rho_{sg}(P_g)$$

$$A_{sl} = A(X_{sl})$$

$$A_{sg} = A(X_{sg})$$

$$\frac{\partial \dot{W}_{2p}}{\partial t} = a_{2p}[P_{2p} - P_g] - b_{2p}\frac{\dot{W}_{2p}^2}{\rho_{av,\,2p}} - c_{2p}\left[\frac{\dot{W}_g^2}{\rho_{sg}} - \frac{\dot{W}_{2p}^2}{\rho_{sl}}\right]$$

$$a_{2p} = a(X_{sl}, X_{sg})$$

$$b_{2p} = b\left(X_{s\ell}, X_{sg}, \dot{W}_{2p}, \frac{\rho_{f,\,2p}}{\rho_{b,\,2p}}\right)$$

$$c_{2p} = c(X_{s\ell}, X_{sg})$$

$$\rho_{av,\,2p} = \frac{2\rho_{s\ell}\rho_{sg}}{\rho_{s\ell} + \rho_{sg}}$$

A two-phase fluid state relation is derived in appendix B. The resulting equation is

$$P_{2p} = \rho_{2p,\,av}\left[\alpha + \beta h_{2p,\,av}\right]$$

where

$$\alpha = \alpha(P_{2p})$$

and

$$\beta = \beta(P_{2p})$$

The gas fluid-lump is bounded by a variable upstream boundary at the saturated-gas interface and by a stationary downstream boundary at the core exit. The defining equations are

$$\frac{\partial}{\partial t}\left[\rho_{g,\,av}V_g\right] = \dot{W}_{2p} - \rho_{sg}A_{sg}U_{B,\,sg} - \dot{W}_g$$

$$V_g = V(X_{sg})$$

$$\frac{\partial \dot{W}_g}{\partial t} = a_g\left[P_g - P_{nc}\right] - b_g\frac{\dot{W}_g^2}{\rho_{av,\,g}} - c_g\left[\frac{\dot{W}_{nc}^2}{\rho_{nc}} - \frac{\dot{W}_g^2}{\rho_{sg}}\right]$$

$$a_g = a(X_{sg})$$

$$b_g = b(X_{sg}, \dot{W}_g)$$

$$c_g = c(X_{sg})$$

$$\rho_{av,\,g} = \frac{2\rho_{sg}\rho_{nc}}{\rho_{sg} + \rho_{nc}}$$

$$P_g = R\rho_{g,\,av}T_{b,\,g}$$

The system-heat-transfer model. - The operation of this part of the overall model is based on the conservation of energy in the components material. The system is considered composed of many lumps. Each lump represents a fixed amount of mass. A typical mass-lump is represented in figure 30.

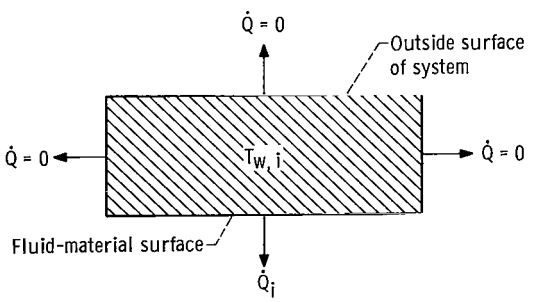

Figure 30. - Typical mass-lump.

Each lump is characterized by an average temperature $T_{w,\,i}$. Conduction from the outside surface to the inside surface is assumed negligible. Consider heat transfer between the metal and fluid only, and assume that the rate of heat loss by the material is balanced by the input heat flux to the fluid.

From a heat balance for such a lump it follows that

$$\frac{\partial T_{w,\,i}}{\partial t} = -\frac{\dot{Q}_i}{M_i c_{p,\,i}}$$

Let $X_{i,1}$ be the distance from $x = 0$ (pump discharge) to one edge of the mass-lump and $X_{i,2}$ be the distance from $x = 0$ to the outer edge. Then

$$\dot{Q}_i = \int_{X_{i,1}}^{X_{i,2}} \dot{Q}'(x, t)dx$$

This calculation will be performed for each lump in the spatial-distribution model. The inputs to this part of the model, therefore, are the individual mass-lump heat fluxes. The outputs are the average wall temperatures.

The system-heat-transfer model is also programmed on the slow-speed analog. This part of the mathematical model considers the system from the nozzle-inlet manifold $x = X_{ni}$ to the thrust-nozzle chamber $x = X_{nc}$. A diagram of the mass lumping is shown as unshaded areas in figure 31. The convergent-divergent nozzle is treated as three

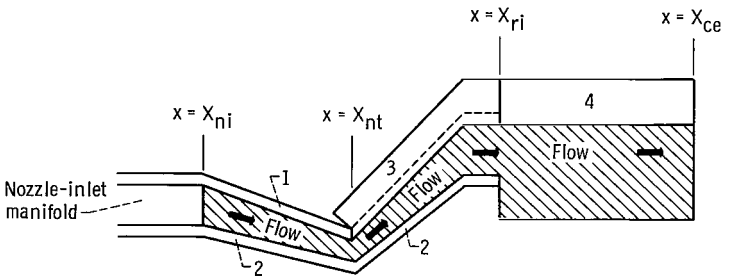

Figure 31. - Mass lumping of system-heat-transfer model.

mass-lumps. One mass-lump is assumed from the reflector inlet to the core exit.

In the diagram the mass-lumps of the convergent-divergent nozzle are labeled 1, 2, and 3. Mass-lump 1 represents the outside nozzle-coolant-tubes material extending from the nozzle-inlet manifold $x = X_{ni}$ to the nozzle-coolant-tubes throat $x = X_{nt}$. From the experimental data, the temperature of this tube material is about equal to the coolant fluid temperature. Hence, no heat flux is assumed in mass-lump 1.

Mass-lump 2 represents the inside nozzle-coolant-tubes material extending the entire length of the tubes. This tube material is in contact with the coolant fluid on one side and with the thrust-nozzle hot gas on the other side. Based on experimental data, no heat-flux storage will be assumed. Hence, the heat flux gained from the hot gas is transferred entirely to the coolant fluid. The average metal temperature is assumed a constant:

$$T_{w,\,hg} = \text{Constant}$$

Mass-lump 3 represents the remaining outside nozzle-coolant-tubes material plus an external metal shell, or skirt. This mass-lump extends from the nozzle-coolant-tubes throat $x = X_{nt}$ to the nozzle-coolant-tubes exit $x = X_{ne}$. The defining equation is

$$\frac{\partial T_{w,\,ns}}{\partial t} = -\frac{\dot{Q}_{ns}}{M_{ns} c_{p,\,ns}}$$

Geometry and mass data for the mass-lumps of the convergent-divergent nozzle are available in reference 7.

The remainder of the system mass is grouped into a gross mass-lump 4. The initial system component composing mass-lump 4 is the reflector. The reflector is a source of high input heat flux. Therefore, it is anticipated that two-phase fluid will not penetrate much into the reflector.

Most of the fluid in mass-lump 4 is assumed to be gas. The total heat flux lost by the mass in this lump is considered transferred to the gaseous fluid. Hence, the defining equation of mass-lump 4 is

$$\frac{\partial T_{w,\,ri\text{-}ce}}{\partial t} = -\frac{\dot{Q}_g}{M_{ri\text{-}ce} c_{p,\,sg\text{-}ce}}$$

The equations and operation of the slow-speed analog have been described. In review, a slow-speed solution is continually generated. Every second of computer operation produces 0.01 second of the solution. The pump speed and nozzle-inlet-manifold fluid enthalpy are programmed from experimental data.

The slow-speed analog requires several inputs from the high-speed analog. These inputs are (1) positions of both two-phase saturated-fluid boundaries, (2) average fluid enthalpy for proper mass-flow storage in the two-phase fluid-lump, (3) average fluid temperature in the gas fluid-lump, (4) thrust-nozzle-chamber fluid temperature, (5) input heat flux from the nozzle-coolant-tubes shell, and (6) input heat flux to the gaseous fluid. A list of these inputs is X_{sl}, X_{sg}, h_{2p}, $T_{b,\,g}$, $T_{b,\,nc}$, $\dot{Q}_{ns}$, and $\dot{Q}_g$.

The slow-speed analog supplies several outputs to the high-speed analog. These outputs are (1) time, (2) nozzle-inlet-manifold pressure, (3) individual fluid-lump flows, (4) saturated-fluid densities, (5) average nozzle-coolant-tubes metal temperature for hot-gas heat transfer, (6) average metal temperature of the nozzle-coolant-tubes shell, and (7) average metal temperature of the region from the reflector inlet to the core exit. A

list of these outputs is t, P_{ni}, $\dot{W}_{\ell}$, $\dot{W}_{2p}$, $\dot{W}_{g}$, $\rho_{s\ell}$, ρ_{sg}, $T_{w,hg}$, $T_{w,ns}$, and $T_{w,\,ri\text{-}ce}$.

The spatial-distribution model. - At some time t this part of the model receives inputs from the slow-speed analog. Spatial-distributions of fluid enthalpy, pressure, density, and input heat flux are rapidly determined. From the distributions, certain quantities are calculated and sent to the slow-speed analog.

At some later time $(t + \Delta t)$, inputs are again received. Spatial distributions are again rapidly determined. And new outputs are calculated for use in the slow-speed analog.

These new outputs represent updated values of the same quantities which were calculated at time t. In the limit as Δt approached zero, the outputs are updated at each instant of time.

This part of the model furnishes the three-fluid-lump model with the positions of the two-phase fluid boundaries in the system. It also supplies an average fluid enthalpy for the two-phase fluid-lump and two fluid temperatures for use in the gas fluid-lump. In return, the individual fluid-lump flows are received as inputs.

Wall material temperatures are also received as inputs. The system-heat-transfer model furnishes these inputs, and receives, in return, evaluations of input heat flux for the individual mass-lumps.

A complete cycle of operation will consist of four steps. The first step is the establishment of all necessary initial conditions. These initial conditions are based on the inputs from the slow-speed analog.

The second step is a continuous high-speed integration with respect to distance. The range of integration is from the nozzle-inlet manifold to the saturated-gas boundary. As a result of the integration, the following slow-speed-analog inputs are determined: (1) the two-phase saturated boundaries $X_{s\ell}$ and X_{sg}, (2) the average two-phase fluid enthalpy $h_{2p,\,av}$ and (3) the input heat flux from shell of the nozzle-coolant tubes $\dot{Q}_{ns}$.

The third step of the operation cycle begins with the termination of the high-speed integration. The core-exit fluid temperature $T_{b,\,ce}$ is calculated from a heat balance on the gaseous fluid. The average values of the gas temperature $T_{b,\,g}$ and input heat flux $\dot{Q}_{g}$ are also determined. At the end of this step, with all the spatial-distribution-model calculations completed, the new values are tracked, or sampled. The analog circuits (ref. 8) remain in the tracking mode only long enough to completely establish the new values. A typical output from a track-and-store circuit could take the form shown in figure 32.

In the final step, information is transferred from the high-speed analog to the slow-speed analog, from the track-and-store circuits. The information remains stored until new values are calculated. The slow-speed analog inputs are transferred as soon as they are calculated. For example, one of the spatial distributions generated is that of fluid enthalpy h(x). During the high-speed integration, h continually increases from its initial value of h_{ni} to its final value of h_{sg}. At some point $(x = X_{s\ell})$ h will pass

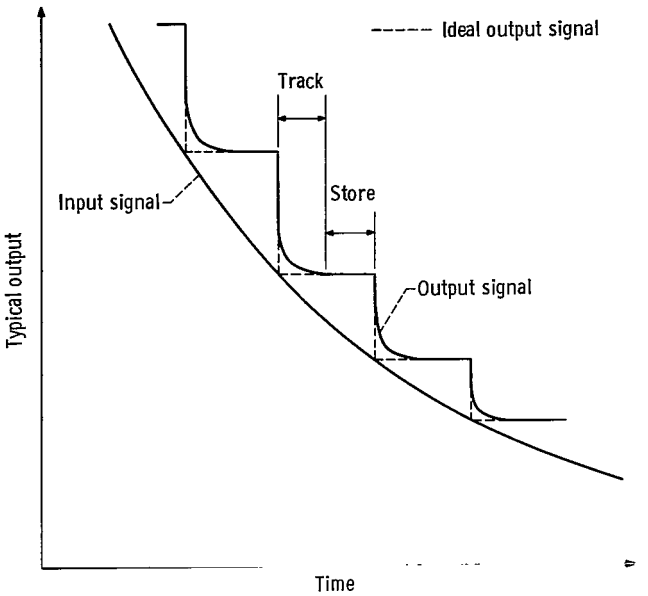

Figure 32. - A typical output from a track-and-store circuit (greatly exaggerated).

through the value of $h = h_{sl}$. The instant that this occurs, a track-and-store circuit is triggered to track the value of x. The new position of the saturated-liquid fluid boundary $x = X_{sl}$, therefore, will be stored.

The spatial-distribution model considers the system from the nozzle-inlet manifold ($x = X_{ni}$) to the core exit ($x = X_{ce}$). A diagram of the flow passages comprising the lump used in the simplified analog program is shown as the shaded areas in figure 31.

The heat-transfer equations pertaining to the fluid in the nozzle-coolant tubes are based on the material presented in reference 7. Some of the expressions, of course, reflect assumptions already made for the slow-speed analog equations.

The differential equations for the spatial-distribution model are developed in appendix C. The energy equation is

$$\frac{\partial h}{\partial x}(x, t) = \frac{\dot{Q}'(x, t) + A(x)\varphi(x, t)\dfrac{\partial P_{2p}}{\partial t}}{\dot{W}(x, t)}$$

where

$$\varphi(x, t) = \varphi_{\ell}(h, P_{ni}) \qquad \text{for } h(x, t) < h_{s\ell}(x, t)$$

$$= \varphi_{2p}(h, P_{2p}) \qquad \text{for } h_{s\ell}(x, t) \leq h(x, t) \leq h_{sg}(x, t)$$

subject to the initial condition

$$h(X_{ni}, t) = h_{ni}(t) = h_{ni}$$

The time derivative is approximated with an analog derivative circuit.

The approximate pressure equation is

$$\frac{\partial P}{\partial x}(x, t) = -\frac{\pi D \tau_w}{nA}(x, t)$$

The initial condition for this expression is supplied by the slow-speed analog and is

$$P(X_{ni}, t) = P_{ni}(t) = P_{ni}$$

The flow is assumed uniform in each fluid-lump of the slow-speed analog. Hence, the following discontinuous flow distribution is assumed:

$$\dot{W}(x, t) = \dot{W}_{\ell} \qquad \text{for } h(x, t) < h_{s\ell}(x, t)$$

$$= \dot{W}_{2p} \qquad \text{for } h_{s\ell}(x, t) \leq h_{(x, t)} \leq h_{sg}(x, t)$$

$$= \dot{W}_{g} \qquad \text{for } h(x, t) > h_{sg}(x, t)$$

The saturated-liquid fluid enthalpy $h_{s\ell}$ is strictly a function of pressure. Because of a spatial pressure distribution, however, an equation may be written:

$$h_{s\ell}(P) = h_{s\ell}(x, t)$$

As in the slow-speed analog, the saturated-gas fluid enthalpy h_{sg} is considered a constant.

An expression for the effective wall shear τ_w for turbulent flow with Reynolds numbers less than 200 000 is (ref. 5)

$$\tau_w = \frac{1}{2g} f_b \rho_b U_b^2 = 0.023 \left[\frac{\mu_f A}{\dot{W} D}\right]^{0.2} \frac{\dot{W}^2}{\rho_b A^2}$$

Bend and entrance effects may be included in an additional loss term. The effective wall shear becomes

$$\tau_w = \frac{0.023}{g} \left[\frac{\mu_f A}{\dot{W} D}\right]^{0.2} \frac{\dot{W}^2}{\rho_b A^2} \frac{D}{L} \left[\frac{L}{D} + K_{loss}\right]$$

$$= \frac{0.023}{g A L} \left[\frac{D}{A}\right]^{0.8} \left[\frac{L}{D}\right]_{eff} \left[\frac{\mu_f}{\dot{W}}\right]^{0.2} \frac{\dot{W}^2}{\rho_b}$$

For the case when variations in fluid viscosity are small,

$$\frac{\partial P}{\partial x}(x, t) = - \frac{K_{fr}(x) \dot{W}^{1.8}(x, t)}{\rho(x, t)}$$

where

$$K_{fr}(x) = \frac{0.023 \pi D \mu_f^{0.2}}{n g A^2 L} \left[\frac{D}{A}\right]^{0.8} \left[\frac{L}{D}\right]_{eff}$$

In the liquid phase, the fluid density ρ is approximated by its saturated-liquid value. In the two-phase fluid, the state relation derived in appendix B is used. For the spatial-distribution model, therefore, the fluid density is

$$\rho(x, t) = \rho_{sl}(x, t) \qquad \text{for } h(x, t) < h_{sl}(x, t)$$

$$= \frac{P(x, t)}{\alpha(P) + \beta(P) h(x, t)} \qquad \text{for } h_{sl}(x, t) \leq h(x, t) \leq h_{sg}(x, t)$$

The input heat flux per unit length $\dot{Q}'(x)$ takes on three basic forms. The describing equation is

$$\dot{Q}'(x,t) = \dot{Q}'_{hg}(x,t) \qquad \text{for } X_{ni} \le x \le X_{nt}$$

$$= \dot{Q}'_{hg}(x,t) + \dot{Q}'_{ns}(x,t) \qquad \text{for } X_{nt} \le x \le X_{ri}$$

$$= \dot{Q}'_{r}(x,t) \qquad \text{for } X_{ri} \le x \le X_{re}$$

where $\dot{Q}'_{hg}(x,t)$ is the input heat flux per unit length from the hot gas on the thrust side of nozzle, $\dot{Q}'_{ns}(x,t)$ is the input heat flux per unit length from the nozzle-coolant-tubes shell, and $\dot{Q}'_{r}(x,t)$ is the input heat flux per unit length from the reflector passages.

The equation for hot-gas input heat flux is

$$\dot{Q}'_{hg} = \mathscr{H}_{hg} A'_{ht,\,hg} [T_{b,\,nc} - T_{w,\,hg}]$$

where $A'_{ht,\,hg}$ is the hot-gas heat-transfer area per unit length. The hot-gas heat-transfer coefficient $\mathscr{H}_{hg}$ will be similar to that used in reference 7. The expression for the coefficient is

$$\mathscr{H}_{hg} = C_{hg} \frac{k_f}{D} Re_f^{0.8} Pr_f^{0.4}$$

where

$$Re_f = \frac{\dot{W} D}{\mu_f A}$$

The input heat-flux equation, therefore, may be written as

$$\dot{Q}'_{hg}(x,t) = K_{hg}(x) F_{hg} \dot{W}^{0.8}(x,t) [T_{b,\,nc} - T_{w,\,hg}]$$

where

$$K_{hg} = \frac{C_{hg}}{D}\left[\frac{D}{A}\right]^{0.8} A'_{ht,\,hg}$$

$$F_{hg} = [k\mu^{-0.8}Pr^{0.4}]_{T_b=T_{f,\,hg}}$$

and

$$T_{f,\,hg} = \frac{T_{w,\,hg} + T_{b,\,nc}}{2}$$

The fluid-properties coefficient F_{hg} is evaluated at an average, constant value of pressure. The geometry coefficient $C_{hg}(x)$ was obtained from reference 7.

The nozzle-coolant-tubes wall between the hot-gas and the coolant is assumed to be at a constant temperature $T_{w,\,hg}$. By assuming no heat-flux storage in the wall $\dot{Q}_{hg}$ may be calculated and applied to the coolant side of the nozzle. Hence, no complicated two-phase boiling heat-transfer coefficient is required.

The input heat flux from the nozzle-coolant-tubes shell $\dot{Q}_{ns}$ however, requires the use of a boiling heat-transfer coefficient. The convective film boiling heat-transfer coefficient from reference 9 is used. The correlation is for liquid hydrogen in the pressure range 25 to 175 psia (172 to 2107 kN/m^2). In terms of the Martinelli parameter χ_{tt}, the correlation is

$$\frac{Nu_{exp,\,f}}{Nu_{calc,\,fm}} = \frac{1}{0.7 + 2.4\,\chi_{tt}} + 0.15$$

where

$$Nu_{exp,\,f} = \frac{\mathcal{H}D}{k_f}$$

$$Nu_{calc,\,fm} = 0.021\left[\frac{\rho_{fm}D\dot{W}}{\rho_b A\mu_f}\right]^{0.8} Pr_f^{0.4}$$

$$\frac{1}{\rho_{fm}} = \frac{X_q}{\rho_f} + \frac{1 - X_q}{\rho_{s\ell}}$$

$$T_f = \frac{T_w + T_b}{2}$$

and

$$\chi_{tt} = \left[\frac{1-X_q}{X_q}\right]^{0.9} \left[\frac{\rho_f}{\rho_{s\ell}}\right]^{0.5} \left[\frac{\mu_{s\ell}}{\mu_f}\right]^{0.1}$$

The input heat flux per unit length from the nozzle-coolant-tubes shell is

$$\dot{Q}'_{ns} = \mathcal{H}_{ns} A'_{ht,\,ns} [T_{w,\,ns} - T_{b,\,ns}]$$

where $A'_{ht,\,ns}$ is the heat-transfer area per unit length. The bulk fluid temperature is given by

$$T_{b,\,ns} = T_{sat}(P)$$

Combining the last six equations results in the following expressions

$$\dot{Q}'_{ns}(x,t) = K_{ns}(x) F_{ns}(x,t) \dot{W}^{0.8}(x,t) [T_{w,\,ns} - T_{b,\,ns}]\,(x,t)$$

where

$$K_{ns} = \frac{0.021}{D} \left[\frac{D}{A}\right]^{0.8} A'_{ht,\,ns}$$

$$F_{ns} = \frac{[k\mu^{-0.8} Pr^{0.4}]_f}{\rho_b^{0.8}} \left\{\frac{\rho_{s\ell}\rho_f}{X_q\rho_{s\ell} + [1-X_q]\rho_f}\right\}^{0.8} \left[\frac{1.105 + 0.36\,\chi_{tt}}{0.7 + 2.4\,\chi_{tt}}\right]$$

and

$$T_{f,ns} = \frac{T_{w,ns} + T_{b,ns}}{2}$$

The fluid-properties coefficient F_{ns} is evaluated at an average, constant value of film temperature $T_{f,ns}$ at several values of pressure. The final value of F_{ns} is obtained from linear interpolation between the constant-pressure values. The wall temperature $T_{w,ns}$ is an input from the slow-speed analog and is assumed uniform throughout the nozzle-coolant-tubes shell.

The overall nozzle shell input heat flux $\dot{Q}_{ns}$ is the sum of $\dot{Q}'_{ns}$ for the entire length. Hence

$$\dot{Q}_{ns} = \int_{X_{nt}}^{X_{ri}} \dot{Q}'_{ns}(x,t)\,dx$$

When $x = X_{ri}$ during the high-speed integration, this value is stored for use in the slow-speed analog.

The final input heat flux per unit length to be defined is $\dot{Q}'_r$, the value for the two-phase fluid in the reflector passages. It is assumed that the input heat flux per unit length of the reflector-inlet manifold is approximately the same as that in the reflector passages. Two-phase film boiling is assumed. The defining equations are similar to those for the nozzle-coolant-tubes shell; that is,

$$\dot{Q}'_r(x,t) = K_r(x)\,F_r(x,t)\dot{W}^{0.8}(x,t)[T_{w,r} - T_{sat}](x,t)$$

where

$$K_r = \frac{0.023}{D}\left[\frac{D}{A}\right]^{0.8} A'_{ht,r}$$

$$F_r = \frac{[k\mu^{-0.8}Pr^{0.4}]_f}{\rho_b^{0.8}}\left\{\frac{\rho_{sl}\rho_f}{X_q\rho_{sl} + [1-X_q]\rho_f}\right\}^{0.8}\left[\frac{1.105 + 0.36\,\chi_{tt}}{0.7 + 2.4\,\chi_{tt}}\right]$$

$$T_{f,r} = \frac{T_{w,r} + T_{sat}}{2}$$

and

$$T_{w,r} = T_{w,ri\text{-}ce} - \Delta T_{r,2p}$$

The fluid properties coefficient F_r is evaluated at an average, constant film temperature $T_{f,r}$ at several values of pressure. The final value of F_r is obtained from a linear interpolation between the constant-pressure values.

As discussed earlier, two-phase fluid is found just inside the reflector. The temperature of the reflector material in contact with the two-phase fluid is $T_{w,r}$. The $T_{w,r}$ is assumed to be lower than the average wall temperature $T_{w,ri\text{-}ce}$ by a fixed amount $\Delta T_{r,2p}$. The $T_{w,ri\text{-}ce}$ is the temperature of mass-lump 4 in the slow-speed analog. This is a good approximation as shown in figure 16. The difference between the predicted $T_{w,ri\text{-}ce}$ and the experimental reflector-inlet fluid temperature tends to remain constant.

The high-speed integration ends at the saturated-gas boundary $x = X_{sg}$. The remainder of the system contains gaseous fluid. A general equation for the overall input heat flux to the fluid is

$$\dot{Q}_g = \mathcal{H}_g A_{ht,g}[T_{w,ri\text{-}ce} - T_{b,g}]$$

The conventional correlation of reference 5 for gaseous hydrogen flow is used; that is,

$$Nu_b = 0.023\, Re_b^{0.8} Pr_b^{0.4}$$

Combining the two previous equations and then grouping terms yields the following relation for the overall, gaseous-fluid, input heat flux:

$$\dot{Q}_g(X_{sg}, t) = C_{ht,g}(X_{sg}) F_g \dot{W}_g^{0.8}[T_{w,ri\text{-}ce} - T_{b,g}]$$

where

$$C_{ht,\,g} = \sum_{x=X_{sg}}^{X_{ce}} \left[\frac{0.023\,A_{ht}}{D^{0.2}A^{0.8}}\right]_x$$

$$F_g = [k\mu^{-0.8}Pr^{0.4}]_{T_b=T_{b,\,g,\,av}}$$

$$T_{b,\,g,\,av} = \frac{T_{sat} + T_{b,\,ce}}{2}$$

and

$$T_{sat} = T_{sat}(P_g)$$

The derivation of the effective-geometry coefficient $C_{ht,\,g}$ is presented in appendix A. The fluid-properties coefficient F_g is assumed a constant; its value is determined from average, constant experimental values of $T_{b,\,g,\,av}$ and gas pressure.

The input heat flux per unit length Q'_g is required. An approximate expression is

$$\dot{Q}'_g = \frac{\dot{Q}_g}{X_{ce} - X_{sg}}$$

The only remaining term to be evaluated is the thrust-nozzle-chamber fluid temperature $T_{b,\,nc}$. The core-exit fluid temperature may be obtained from an energy balance on the gaseous fluid. A simplified finite-difference form of the general energy equation found in appendix E is used. Neglecting the time derivatives and assuming uniform flow,

$$\dot{W}_g \left[\frac{\Delta h}{\Delta x}\right]_g \approx \dot{Q}'_g$$

This equation may be rewritten as

$$\dot{W}_g c_{p,g} \left[\frac{T_{b,ce} - T_{sat}}{X_{ce} - X_{sg}} \right] = \dot{Q}'_g$$

The thrust-nozzle-chamber fluid temperature may be approximated by the value of the core-exit fluid temperature; that is,

$$T_{b,nc} \approx T_{b,ce} = T_{sat} + \frac{\dot{Q}_g(X_{sg}, t)}{\dot{W}_g c_{p,g}}$$

The specific heat $c_{p,g}$ is evaluated at an average, constant value of fluid temperature.

The description of the high-speed analog is nearly complete. The necessary equations for the high-speed solution have been presented. The averaging procedure for $h_{2p,av}$, the average two-phase enthalpy, however, remains to be described. Assume that this averaging is not required in the gas fluid-lump.

To obtain proper mass-flow storage in the gross two-phase fluid-lump an average value of the thermodynamic property $[\partial\rho/\partial P]_h$ is required. This phenomenon was discussed earlier in appendix A. Constant-pressure curves of $[\partial\rho/\partial P]_h$ against fluid enthalpy are derivable from hydrogen properties tables (ref. 3).

Spatial distributions of fluid enthalpy h and fluid pressure P are continuously generated every cycle. By linearily interpolating on pressure, a continuous distribution of $[\partial\rho/\partial P]_h$ is derived from the enthalpy distribution. Hence,

$$\left[\frac{\partial\rho}{\partial P}\right]_h = \left[\frac{\partial\rho}{\partial P}\right]_h (h, P) = \left[\frac{\partial\rho}{\partial P}\right]_h (x, t)$$

is known.

The average value of this thermodynamic property for the two-phase fluid-lump would be

$$\left[\frac{\partial\rho}{\partial P}\right]_{h,av} = \frac{\int_{X_{s\ell}}^{X_{sg}} \left[\frac{\partial\rho}{\partial P}\right]_h (x, t)\,dx}{X_{sg} - X_{s\ell}}$$

Therefore, the average two-phase fluid enthalpy for proper mass-flow storage is

$$h_{2p,\,av} = h\left(P_{2p},\left[\frac{\partial\rho}{\partial P}\right]_{h,\,2p,\,av}\right)$$

This required property of enthalpy as a function of pressure and $[\partial\rho/\partial P]_h$ is derivable from the curves in reference 3.

The high-speed analog requires several inputs from the slow-speed analog. The inputs are (1) time, (2) nozzle-inlet-manifold pressure, (3) individual fluid-lump flows, (4) saturated-fluid densities, (5) average nozzle-coolant-tubes metal temperature for hot-gas heat transfer, (6) average metal temperature of the nozzle-coolant-tubes shell, and (7) average metal temperature of the reflector-to-core-exit region. A list of these inputs is t, P_{ni}, $\dot{W}_{\ell}$, $\dot{W}_{2p}$, $\dot{W}_g$, $\rho_{s\ell}$, ρ_{sg}, $T_{w,\,hg}$, $T_{w,\,ns}$, and $T_{w,\,ri\text{-}ce}$.

The high-speed analog supplies several outputs to the slow-speed analog. These outputs are (1) the positions of both two-phase saturated fluid boundaries, (2) the average fluid enthalpy for proper mass-flow storage in the two-phase fluid-lump, (3) the average gas-fluid-lump temperature, (4) the thrust-nozzle-chamber fluid temperature, (5) the input heat flux from the nozzle-coolant-tubes shell, and (6) the input heat flux to the gaseous fluid. A list of these outputs is $X_{s\ell}$, X_{sg}, $h_{2p,\,av}$, $T_{b,\,g}$, $T_{b,\,nc}$, $\dot{Q}_{ns}$, and $\dot{Q}_g$.

Each cycle of operation begins with the establishment of initial conditions. These conditions are based on inputs from the slow-speed analog. During the subsequent high-speed x-integration, updated values for $X_{s\ell}$, X_{sg}, $h_{2p,\,av}$, $\dot{Q}_{ns}$ are formed and stored in analog track-and-store circuits. And finally, new values for $T_{b,\,g}$, $T_{b,\,nc}$, and $\dot{Q}_g$ are calculated and sent to the slow-speed analog.

Thrust Nozzle

The analog model is terminated by a thrust-nozzle lump. The thrust nozzle is assumed to be choked. The defining equations are

$$\frac{\partial\rho_{nc}}{\partial t} = \frac{\dot{W}_g - \dot{W}_{nc}}{V_{nc}}$$

$$\dot{W}_{nc} = \frac{K_{nc}P_{nc}}{\sqrt{T_{b,\,nc}}}$$

and

$$P_{nc} = R\rho_{nc}T_{b,nc}$$

APPENDIX E

SPATIAL-DISTRIBUTION MODEL EQUATIONS

A set of general, one-dimensional differential equations based on the conservation of mass, momentum, and energy, respectively, in circular passages is as follows:

$$\frac{\partial \rho}{\partial t} + \frac{1}{A}\frac{\partial \dot{W}}{\partial x} = 0$$

$$\frac{1}{A}\frac{\partial \dot{W}}{\partial t} + \frac{\partial}{\partial x}\left[ngP + \frac{\dot{W}^2}{\rho A^2}\right] = -\frac{\pi D g \tau_w}{A}$$

$$\frac{\partial}{\partial t}[\rho h - J'P] + \frac{1}{A}\frac{\partial}{\partial x}[\dot{W}h] = \frac{\dot{Q}'}{A}$$

Combining the mass and energy equation yields

$$\rho\frac{\partial h}{\partial t} - J'\frac{\partial P}{\partial t} + \frac{\dot{W}}{A}\frac{\partial h}{\partial x} = \frac{\dot{Q}'}{A}$$

Solving for the spatial gradient yields

$$\frac{\partial h}{\partial x} = \frac{\dot{Q}' + A\left[J'\frac{\partial P}{\partial t} - \rho\frac{\partial h}{\partial t}\right]}{\dot{W}}$$

Neglecting mass-flow storage results in

$$\frac{\partial h}{\partial t} \approx \left[\frac{\partial h}{\partial P}\right]_\rho \frac{\partial P}{\partial t}$$

since

$$\frac{\partial \rho}{\partial t} = -\frac{1}{A}\frac{\partial \dot{W}}{\partial x} \approx 0$$

The enthalpy spatial gradient for fluid-lump, therefore, becomes

$$\frac{\partial h}{\partial x}(x,t) = \frac{\dot{Q}'(x,t) + A(x)\varphi(x,t)\frac{\partial P}{\partial t}(x,t)}{\dot{W}(x,t)}$$

where

$$\varphi(x,t) = J' - \rho(x,t)\left[\frac{\partial h}{\partial P}\right]_{\rho}(x,t)$$

and, to a first approximation,

$$\frac{\partial P}{\partial t}(x,t) \approx \frac{\partial P}{\partial t}(t) = \frac{\partial P_{2p}}{\partial t}$$

For the pressure ranges in this study the pressure dependence of the saturated-gas fluid enthalpy may be neglected (ref. 3). The pressure dependence of the saturated-liquid enthalpy, however, is important. The pressure-drop equation is integrated with respect to x in repetitive operation solely to supply this pressure dependence. Therefore, to generate an approximate two-phase pressure distribution and, at the same time, minimize the necessary amount of analog computing equipment, only friction pressure drop is considered; that is,

$$\frac{\partial P}{\partial x}(x,t) = -\frac{\pi D \tau_w}{nA}(x,t)$$

APPENDIX F

SYMBOLS

A	flow area, ft^2; m^2
A'_{ht}	heat-transfer area per unit length, ft^2/ft; m^2/m
a	effective-geometry coefficient, $(lbm)(in.^2)/(lbf)(sec^2)$; $(kg)(m^2)/(N)(sec^2)$
b	effective-geometry coefficient, ft^{-3}; m^{-3}
C	geometry coefficient
c	effective-geometry coefficient, ft^{-3}; m^{-3}
c_p	specific heat of hydrogen at constant pressure, $Btu/(lbm)(^oR)$; $J/(g)(K)$
D	diameter, ft; m
F	fluid properties coefficient, $Btu/(lbm^{0.8})(ft^{0.2})(sec^{0.2})(^oR)$; $kJ/(kg^{0.8})(m^{0.2})(sec^{0.2})(K)$
f	coefficient of friction
g	gravitational acceleration, 32.174 $(lbm)(ft)/(lbf)(sec^2)$; 1 $(kg)(m)/(N)(sec^2)$
$\mathcal{H}$	heat-transfer coefficient
h	specific enthalpy, Btu/lbm; J/g
J'	conversion factor, $(144\ in.^2/ft^2)/(778\ ft\text{-}lbf/Btu)$
K	heat-transfer geometry coefficient
K_{loss}	pressure loss coefficient for bends and entrance effects
k	thermal conductivity of hydrogen, $Btu/(ft)(sec)(^oR)$; $kJ/(m)(sec)(K)$
L	length, ft; m
l	number of sublumps
M	mass, lbm; kg
m	pump-map slope, $(lbf)(sec)/(lbm)(in.^2)(rpm)$; $(N)(sec)/(kg)(m^2)(rpm)$
N	speed, rpm
Nu	Nusselt number
Nu_{calc}	calculated Nusselt number for two-phase flow
Nu_{exp}	experimental Nusselt number for two-phase flow
n	conversion factor, $144\ in.^2/ft^2$

P	pressure, psia; N/m^2
Pr	Prandtl number
$\dot{Q}$	input heat flux, Btu/sec; kJ/sec
$\dot{Q}'$	input heat flux per unit length, Btu/(ft)(sec); kJ/(m)(sec)
R	specific gas law constant for hydrogen, 5.326 $ft^3/(in.^2)(^oR)$; 420.8 m/K
Re	Reynolds number
T	temperature, ^oR; K
t	time, sec
U	velocity, ft/sec; m/sec
V	volume, ft^3; m^3
v	specific volume, ft^3/lbm; m^3/kg
$\dot{W}$	mass-flow rate, lbm/sec; kg/sec
X	distance (finite length), ft; m
X_q	mass quality
x	distance (independent variable), ft; m
Z	height, ft; m
α	two-phase state-equation coefficient, $(lbf)(ft^3)/(lbm)(in.^2)$ abs; (N)(m)/kg
β	two-phase state-equation coefficient, $(lbf)(ft^3)/(Btu)(in.^2)$ abs; (N)(m)/kg
μ	viscosity, (lbm)/(ft)(sec); kg/(m)(sec)
ρ	fluid density, lbm/ft^3; kg/m^3
ρ'_{av}	average (linear) fluid density, lbm/ft^3; kg/m^3
τ	effective shear, lbf/ft^2; (N/m^2)
φ	heat-transfer function, $(Btu)(in.^2)/(lbf)(ft^3)$
χ_{tt}	Martinelli two-phase parameter

Subscripts:

av	average
B	boundary
b	bulk
ce	core exit

ci	core inlet
e	error
eff	effective
f	film
fm	film mean
fr	friction
g	gas
gr	gravity
h	enthalpy
hg	hot gas
ht	heat transfer
i	sublump number
in	inlet of flow stage
iner	inertia
l	liquid
loss	loss
mfcv	main flow-control valve
mom	momentum
n	nozzle
nc	thrust-nozzle chamber
ne	nozzle-coolant-tubes exit
ni	nozzle-coolant-tubes inlet
ns	nozzle-coolant-tubes shell
nt	nozzle-coolant-tubes throat
out	outlet of flow stage
P	pressure
p	pump
pi	pump inlet
po	pump outlet
r	reflector

re	reflector exit
ri	reflector inlet
sat	saturated
se	spider exit
sg	saturated gas
sl	saturated liquid
t	tank
tot	total
w	wall
wb	wall to bulk
x	distance
2p	two-phase

REFERENCES

1. Heppler, Herbert J., Jr.; Colmery, Benjamin H.; Watt, James J.; and Gebben, Vernon D.: Startup Dynamics and Control. Nuclear Rocket Technology Conference. NASA SP-123, 1966, pp. 105-117.

2. Reardon, John E.: Full-Scale Nuclear Rocket Cold-Flow Test Facility and Research Apparatus. NASA TM X-1763, 1969.

3. Goldberg, Fredric N.; and Haferd, Angela M.: Numerical Procedures for Calculating Real Fluid Properties of Normal and Parahydrogen. NASA TN D-4341, 1968.

4. Maulbetsch, John S.; and Griffith, Peter: System-Induced Instabilities in Forced-Convection Flows with Subcooled Boiling. Third International Heat Transfer Conference. Vol. 4. AIChE, 1966, pp. 247-257.

5. McAdams, William H.: Heat Transmission. Third ed., McGraw-Hill Book Co., Inc., 1954.

6. Humble, Leroy V.; Lowdermilk, Warren H.; and Desmon, Leland G.: Measurements of Average Heat-Transfer and Friction Coefficients for Subsonic Flow of Air in Smooth Tubes at High Surface and Fluid Temperatures. NACA Rep. 1020, 1951.

7. Turney, George E.; and Cox, Eileen: Cooldown Characteristics of Regenerative Nozzle Used in Full-Scale, Cold-Flow, Nuclear Rocket Test Facility. NASA TN D-3931, 1967.

8. Carlson, Alan; and Hannauer, George: Handbook of Analog Computation. Second ed., Electronic Associates, Inc., 1965.

9. Hendricks, Robert C.; Graham, Robert W.; Hsu, Yih Y.; and Friedman, Robert: Experimental Heat-Transfer Results for Cryogenic Hydrogen Flowing in Tubes at Subcritical and Supercritical Pressures to 800 Pounds per Square Inch Absolute. NASA TN D-3095, 1966.

NASA-Langley, 1969 —— 22 E-4856